On the initiation of sustained slip-weakening ruptures by localized stresses

M. Galis,[1] C. Pelties,[2] J. Kristek,[3,4] P. Moczo,[3,4] J.-P. Ampuero[5] and P. M. Mai[1]

[1]*Division of Physical Sciences and Engineering, KAUST, Thuwal 23955-6900, Saudi Arabia. E-mail: martin.galis@kaust.edu.sa*
[2]*Geophysics Section, Department of Earth and Environmental Sciences, Ludwig-Maximilians-University, D-80333 Munich, Germany*
[3]*Faculty of Mathematics, Physics and Informatics, Comenius University Bratislava, Mlynska dolina F1, 842 48 Bratislava, Slovakia*
[4]*Geophysical Institute, Slovak Academy of Sciences, Dubravska cesta 9, 845 28, Bratislava, Slovakia*
[5]*California Institute of Technology, Seismological Laboratory, Pasadena, CA 91125, USA*

SUMMARY

Numerical simulations of dynamic earthquake rupture require an artificial initiation procedure, if they are not integrated in long-term earthquake cycle simulations. A widely applied procedure involves an 'overstressed asperity', a localized region stressed beyond the static frictional strength. The physical properties of the asperity (size, shape and overstress) may significantly impact rupture propagation. In particular, to induce a sustained rupture the asperity size needs to exceed a critical value. Although criteria for estimating the critical nucleation size under linear slip-weakening friction have been proposed for 2-D and 3-D problems based on simplifying assumptions, they do not provide general rules for designing 3-D numerical simulations. We conduct a parametric study to estimate parameters of the asperity that minimize numerical artefacts (e.g. changes of rupture shape and speed, artificial supershear transition, higher slip-rate amplitudes). We examine the critical size of square, circular and elliptical asperities as a function of asperity overstress and background (off-asperity) stress. For a given overstress, we find that asperity area controls rupture initiation while asperity shape is of lesser importance. The critical area obtained from our numerical results contrasts with published theoretical estimates when background stress is low. Therefore, we derive two new theoretical estimates of the critical size under low background stress while also accounting for overstress. Our numerical results suggest that setting the asperity overstress and area close to their critical values eliminates strong numerical artefacts even when the overstress is large. We also find that properly chosen asperity size or overstress may significantly shorten the duration of the initiation. Overall, our results provide guidelines for determining the size of the asperity and overstress to minimize the effects of the forced initiation on the subsequent spontaneous rupture propagation.

Key words: Numerical solutions; Earthquake dynamics; Computational seismology.

1 INTRODUCTION

Earthquakes are associated with rupture propagation on a seismic fault. When the fault is exposed to slow tectonic loading rupture naturally nucleates at its weakest point—the location where the strength equals the 'initial' stress (i.e. the stress at the onset of rupture induced by tectonic loading and previous slip). While the understanding of the earthquake nucleation process is of fundamental importance for earthquake physics (Uenishi & Rice 2003; Rubin & Ampuero 2005; Ampuero & Rubin 2008) studies focused on fast dynamic rupture processes often adopt simplifying assumptions about earthquake nucleation.

Because of limited possibilities for direct observations of real ruptures, many studies of earthquake dynamics are based on numerical simulations. A modern trend in computational earthquake dynamics promotes simulations that include long-term deformation over multiple earthquake cycles (e.g. Barbot *et al.* 2012). In that approach nucleation is spontaneous, mechanically consistent and the physics of nucleation is fully considered. However, the simpler and less computationally costly approach of simulating single earthquake ruptures is still appropriate to study both fundamental aspects of earthquake physics and to utilize dynamic rupture simulation for ground-motion prediction (e.g. Ripperger *et al.* 2007, 2008). In such cases, artificial procedures are used to initiate a self-sustained rupture. Here, we use the term 'initiation' to distinguish an artificial procedure from natural nucleation of an earthquake.

An overstressed asperity—defined as a localized region where the initial shear traction is prescribed to exceed the static fault

strength—is an initiation procedure often applied in dynamic models that adopt the linear slip-weakening friction law (e.g. Duan & Oglesby 2006; Ripperger *et al.* 2007, 2008; Dalguer & Day 2009; Brietzke *et al.* 2009; Pelties *et al.* 2013) or velocity- and state-dependent friction laws with a static strength threshold (e.g. Ampuero & Ben-Zion 2008). Wide recognition of this initiation procedure is also indicated by its use in several SCEC/USGS dynamic earthquake rupture code verification exercises (Harris *et al.* 2009). An overstressed asperity, or 'initiation zone (IZ)', is defined by prescribing its size, shape and overstress (the difference between the static strength and the initial traction inside the asperity).

Previous studies discuss a variety of options for setting the initiation parameters, but also reveal that the size of the IZ strongly influences the subsequent rupture propagation. Using a too large IZ may lead to, for example, a forced transition from sub-Rayleigh to supershear rupture speed (e.g. Liu & Lapusta 2008) while a too small IZ leads to premature rupture arrest. Therefore, it is important to appropriately choose the size of the IZ. Although different criteria for estimating nucleation size were previously proposed for the 2-D problem (e.g. Andrews 1976a,b; Campillo & Ionescu 1997; Favreau *et al.* 1999; Uenishi & Rice 2003) and the 3-D problem (e.g. Day 1982; Favreau *et al.* 2002; Uenishi & Rice 2004), these do not provide general rules for designing numerical simulations (e.g. Bizzarri 2010; Galis *et al.* 2010).

In addition, various shapes of the IZ were used in previous studies. For example, a square shape was selected because it can be applied in the largest number of numerical methods (e.g. Harris *et al.* 2009). On the other hand, an elliptical shape (e.g. Uenishi & Rice 2004; Dunham 2007) was motivated by considering two physical aspects: (1) the estimates of the nucleation size for the in-plane and antiplane modes are different and (2) soon after initiation, the rupture becomes elliptical, regardless of the shape of the IZ. Bizzarri (2010), inspired by the approach of Day (1982), tested a circular IZ. Ripperger *et al.* (2007) used complex-shaped initiation zones whose exact shapes were determined by the underlying heterogeneous stress pattern and the area needed to achieve spontaneous dynamic rupture propagation.

The overstress is usually assumed not to exceed 1 per cent of the static strength drop and is typically applied as a discontinuity of initial stress at the rim of the IZ. Two recent studies applied a smooth spatial distribution of initial stress (Bizzarri 2010; Galis *et al.* 2010).

In contrast to previous theoretical studies on rupture initiation, we are here interested in self-sustained ruptures. Previous works on rupture initiation under slip-weakening friction (e.g. Campillo & Ionescu 1997; Ampuero *et al.* 2002; Uenishi & Rice 2003) established critical length scales for the onset of self-accelerating slip, but did not consider whether the rupture became indefinitely self-sustained or arrested spontaneously at some (possibly large) distance from the nucleation area. The transition from spontaneously arresting to self-sustained ruptures has been studied under slip-weakening friction by Ampuero *et al.* (2006), Viesca & Rice (2012) and Garagash & Germanovich (2012) in 2-D, and by Ripperger *et al.* (2007) in 3-D. Our first goal is to determine the sufficient ('critical') conditions to initiate sustained ruptures, that is, ruptures on faults with uniform background stress that propagate indefinitely unless they encounter a high strength barrier.

To properly study the physics of rupture propagation, it is crucial to understand, and then minimize, the numerical artefacts induced by the artificial initiation on the subsequent spontaneous rupture propagation. Compared to a natural nucleation process driven by slow tectonic loading (e.g. Uenishi & Rice 2003), we expect the

most representative overstressed asperity initiation setting to be a slightly 'overcritical' initiation, that is, one with size and overstress values slightly larger than the critical values required to produce a self-sustained rupture (for a given IZ shape). We therefore define a numerical artefact as a significant difference between a solution and the reference solution obtained for just slightly overcritical initiation. Our second goal here is to determine 'optimal' initiation parameters that lead to short initiation duration (hence lower computational cost) while avoiding numerical artefacts.

Bizzarri (2010) compared three rupture initiation techniques: overstressed asperities of different shapes, forced rupture propagation with constant rupture speed and perturbation of the initial particle velocity field. He showed that the forced rupture propagation with a proper rupture speed leads to gradual transition from the imposed initiation to spontaneous rupture propagation, and that an elliptical overstressed asperity with smooth stress is a valid alternative to the forced-rupture-propagation initiation. He also evaluated the optimal size of the IZ (note however that his definition of 'optimal' differs from ours). While Bizzarri only considered two specific values of the background stress and one value of overstress, we systematically determine the critical and optimal conditions for a broad range of background stress and overstress values.

Here we perform a detailed parametric study and investigate effects of the forced initiation on rupture propagation to define critical and optimal parameters for initiating 3-D spontaneous rupture propagation. We apply different numerical methods to verify our conclusions. We consider different sizes and shapes of the IZ as well as different overstress values. However, for efficiency reasons, we consider a discontinuous change of the initial stress at the rim of the initiation zone. We compare our numerical results with published 2-D and 3-D estimates, and present two new estimates of the critical initiation size that include the effect of overstress.

2 NUMERICAL METHOD AND COMPUTATIONAL MODEL PARAMETERS

2.1 Finite-element (FE) method

We use a FE method to perform a wide range of numerical simulations for this study. The FE method is implemented in a displacement scheme on hexahedral elements, and is 2nd-order accurate in space and time (e.g. Moczo *et al.* 2007; Galis *et al.* 2008; Moczo *et al.* 2014). Computational efficiency is achieved by making use of the restoring-force vector calculated using the e-invariants (Balažovjech & Halada 2006; Moczo *et al.* 2007, 2014). The traction-at-split-node method (e.g. Andrews 1973, 1999; Day 1977) and adaptive smoothing algorithm (Galis *et al.* 2010) are implemented for simulating rupture dynamics.

As we focus on the initiation of the rupture propagation, it is necessary to explain in detail the implementation of the square and elliptical initiation zones in the FE method. The square shape is the most natural shape for the regular hexahedral mesh whereas an ellipse is an example of a more complex shape of the IZ.

2.1.1 *Implementation of a square IZ*

A square IZ with half-length L_i can be defined by the condition

$$\tau_0 = \begin{cases} \tau_0^i & \text{if } |x_s - x| \leq L_i \vee |y_s - y| \leq L_i \\ \tau_0 & \text{otherwise} \end{cases}, \qquad (1)$$
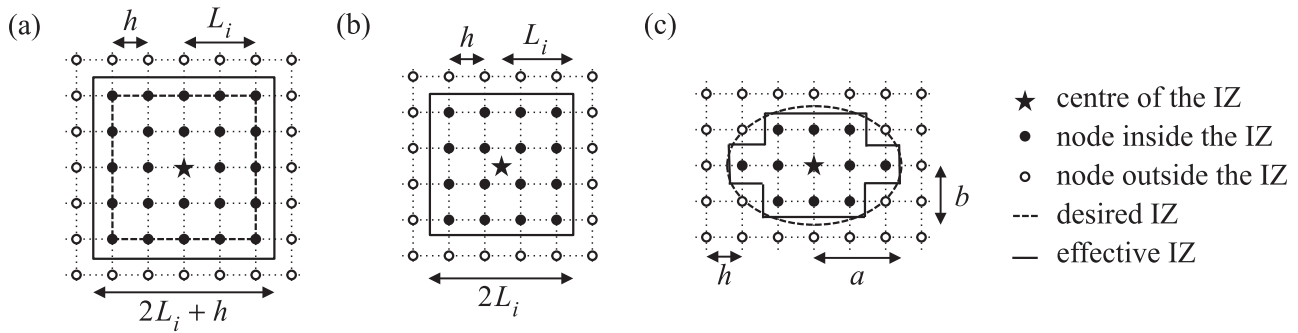
Figure 1. Implementation of an initiation zone (IZ) in the FE mesh: (a) square IZ if hypocentre coincides with a node position, (b) square IZ if hypocentre is in the middle of an element, (c) elliptical IZ. Note that the implementation (a) is used if the size of the IZ is an odd multiple of the element size h, while the implementation (b) is used if the size of IZ is an even multiple of the element size h.

Table 1. Model parameters: μ_s, static coefficient of friction; μ_d, dynamic coefficient of friction; D_c, characteristic distance; τ_0^n, normal component of initial traction (negative for compression); τ_s, static traction; τ_d, dynamic traction; v_p, P-wave speed; v_s, S-wave speed; ρ, density μ; λ, Lamé constants; ν, Poisson's ratio; Q_p, P-wave quality factor; Q_s, S-wave quality factor.

μ_s	μ_d	D_c	τ_n	τ_s	τ_d	v_p	v_s	ρ	$\mu = \lambda$	ν	Q_p, Q_s
0.6778	0.525	0.4 m	−120 MPa	81.333 MPa	63 MPa	6000 m s^{-1}	3464 m s^{-1}	2670 kg m^{-3}	32 GPa	0.25	∞

where τ_0 is the initial traction on the fault, τ_0^i initial traction inside the IZ, x_s and y_s are the hypocentre coordinates (a centre of the IZ).

The square IZ can be exactly represented in a uniform hexahedral mesh only if the length of the square is divisible by the element size h, that is, if the half-length L_i is divisible by $h/2$. Moreover, the hypocentre has to coincide with a node position or with the centre of an element (see Figs 1a and b).

In implementation (a) we assume that the hypocentre coincides with a node position, and construct an IZ with, for example, $L_i = 2h$ (Fig. 1a). In the FE method the friction parameters are defined at nodes. Each node represents a (small) area of the fault surface with the node being in the centre of the area. Therefore, the effective size of the IZ, as obtained from eq. (1), is not $2L_i$ but $2L_i + h$. If the hypocentre coincides with a node position the effective size of the IZ is always an odd multiple of h (also if L_i is not a multiple of h).

In implementation (b) we assume that the hypocentre lies at the centre of an element (Fig. 1b). In this case, eq. (1) yields the effective size $2L_i$, which is always an even multiple of h.

We can choose implementation (a) or (b), whichever results in an effective size closer to the desired size of the IZ. The difference in the hypocentre position in implementations (a) and (b) does not pose a significant problem for simulations as $h/2$ is usually negligible compared to the distances at which we are interested in the rupture propagation. Moreover, later we illustrate that the effect of the incorrect size of IZ is much stronger than a slight shift of the hypocentre position.

The effective size of the IZ is important for simulating dynamic rupture propagation. Therefore, in the remainder of this article we will use the term 'size of the IZ' to refer to the effective size of the IZ in the FE mesh.

2.1.2 Implementation of an elliptical IZ

An elliptical IZ can be defined by the nodes which lie inside the ellipse with semi-axes a and b as

$$\tau_0 = \begin{cases} \tau_0^i & \text{if } \left(\frac{x_s-x}{a}\right)^2 + \left(\frac{y_s-y}{b}\right)^2 \leq 1 \\ \tau_0 & \text{otherwise} \end{cases}. \tag{2}$$

In the case of the uniform hexahedral mesh, the effective IZ is a staircase approximation of the desired elliptical IZ (Fig. 1c). Although smaller elements lead to more accurate representation of the ellipse, it will never be represented exactly in the FE mesh. Therefore, we consider only the case when the hypocentre coincides with a node position.

2.2 Computational model parameters

To numerically investigate the initiation of dynamic rupture propagation we assume a planar fault embedded in an 3-D elastic homogeneous space. We adopt the linear slip-weakening friction law (Ide 1972; Palmer & Rice 1973), and consider a fault plane 30 km long and 15 km wide. Except within the IZ the friction parameters are constant on the fault plane. The friction parameters and medium parameters are specified in Table 1.

The dynamic rupture configuration may be characterized by the non-dimensional strength parameter (Andrews 1976b; Das & Aki 1977)

$$S = \frac{\tau_s - \tau_0}{\tau_0 - \tau_d}, \tag{3}$$

where $\tau_s = \mu_s \tau_n$ and $\tau_d = \mu_d \tau_n$ are the static and dynamic tractions, respectively, τ_n is the normal component of traction and τ_0 is the shear (also tangential or fault-parallel) component of the initial traction. In all configurations we fix static and dynamic coefficients of friction, and assume different values for the initial traction τ_0 to obtain configurations with different values of S.

To correctly discretize the problem for a rupture-dynamics simulation, the resolution of the breakdown zone has to be considered. Day *et al.* (2005) derived estimates of a breakdown-zone width. Their so-called zero-speed estimates apply when rupture speed is very low, that is, shortly after the initiation. Moreover, the zero-speed estimate for mode II (the in-plane mode) is always larger than the zero-speed estimate for mode III (the antiplane mode),

$$\Lambda_0^{\text{III}} = \frac{9\pi}{32} \mu \frac{D_c}{\tau_s - \tau_d}, \tag{4}$$

where μ is a shear modulus and D_c characteristic slip-weakening distance. During rupture propagation the breakdown-zone width

shrinks. Therefore, we consider a sufficiently fine discretization of Λ_0^{III} as a necessary condition. As suggested by Day *et al.* (2005), six or more grid points are necessary for adequately resolving the breakdown zone. Obviously, this applies to their traction-at-split-node implementation of rupture dynamics in the finite-difference method. In our low-order FE method we use a similar implementation of rupture dynamics. Therefore, we may apply Day's sampling also in our simulations. Using parameters in Table 1 we obtain $\Lambda_0^{\mathrm{III}} \approx 617.63$ m leading to a grid spacing (element size) of ~ 100 m or smaller. Note that while the estimate of Λ_0^{III} does not depend on the initial stress τ_0, the dynamic breakdown-zone width does depend on τ_0. Based on our convergence test (see Section 3.3) we choose a grid spacing of $h = 100$ m as the baseline grid spacing. Additionally, we perform some tests also for finer grid spacing, $h = 50$ m.

3 VERIFICATION OF THE FE AND ADER-DG METHODS

We verify our FE method using the arbitrary high-order derivatives–discontinuous Galerkin (ADER-DG) method to demonstrate that our results and conclusions on the initiation parameters are not method dependent.

The ADER-DG method combines ideas of the discontinuous Galerkin methods with the ADER time integration providing high-order accuracy in space and time on unstructured tetrahedral meshes (e.g. Dumbser & Käser 2006; de la Puente *et al.* 2009; Pelties *et al.* 2012, 2013). Mesh refinement in areas of interest or strong mesh coarsening in areas of low importance can be applied to reduce the computational cost. No spurious reflections at the refinement interfaces due to numerical impedance have been observed. Because the order of accuracy $\mathcal{O}$ in the ADER-DG simulations is controlled by the order of the basis functions, the same mesh may be used with various orders of accuracy $\mathcal{O}$. Moreover, the method does not generate spurious high-frequency contributions in the slip-rate spectra of dynamic rupture computations and therefore does not require any artificial Kelvin–Voigt damping or filtering. Note that ADER-DG implemented with the upwind flux is dissipative and the amount of numerical dissipation increases very steeply as a function of frequency. Consequently, very short wavelengths that are poorly resolved by the mesh are adaptively damped without perturbing longer, physically meaningful wavelengths (Pelties *et al.* 2012). However, the price for increased accuracy of the ADER-DG method are higher computational costs compared with the FE method. Therefore, we use the ADER-DG method to verify results obtained with the FE method, and subsequently apply the FE method for extensive simulations. Both methods were applied in previous studies as well as benchmark exercises, and very good agreement with independent methods was found (e.g. Moczo *et al.* 2007; Pelties *et al.* 2012).

In the following, we present a series of numerical tests to show that both methods provide consistent results for the square and elliptical shapes, as well as for different sizes of the IZ. The tests also indicate that the shape of IZ affects convergence properties. For example, for the FE method a square IZ yields more accurate rupture times than an elliptical IZ. On the other hand, for the ADER-DG method an elliptical IZ yields more accurate rupture times.

3.1 Implementation of the IZ in ADER-DG method

Here we briefly summarize principles of implementation of the the IZ in the ADER-DG method. The ADER-DG mesh is prepared
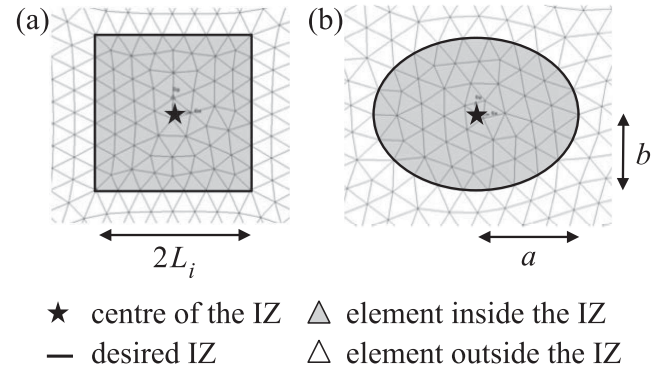

Figure 2. Illustration of a square (a) and elliptical (b) initiation zone (IZ) in the ADER-DG mesh. *Note:* The elliptical initiation zone is represented as piece-wise linear approximation of ellipse, however, the errors are within thickness of the line depicting the desired ellipse.

such that the tetrahedral elements follow the shape (and thus also size) of the IZ as precisely as possible. Because the ADER-DG method uses modal basis functions, the frictional parameters are defined only at the triangular element-faces across the fault (not at the element edges). Consequently, a square IZ is exactly represented (Fig. 2a). However, an elliptical IZ is represented as a piece-wise linear approximation of the desired ellipse (Fig. 2b). If more accurate representation of the ellipse was needed, mesh refinement would be necessary.

3.2 Verification for the square and elliptical initiation zones

Here we compare and validate dynamic-rupture simulations for the square and elliptical initiation zones in the case of $S = 1.0$. Using parameters in Table 1 we obtain $\tau_0 = 72.167$ MPa. The initial traction inside the IZ, τ_0^i, is 81.379 MPa (i.e. the overstress is 0.5 per cent of strength excess, $\Delta\tau_E = \tau_s - \tau_0$). The desired half-length of the square IZ, L_i, is 900 m and the semi-axes of the desired elliptical IZ are $a = 1200$ m and $b = 900$ m, respectively.

For the FE simulations we choose element sizes $h = 100, 50$ and 25 m. Because the desired size of the square IZ ($2L_i = 1800$ m) is an even multiple of any of the considered element sizes, we use implementation (b) to obtain an IZ with a correct effective size (Fig. 1b). Because we are interested in comparing slip-rate time histories, we apply the adaptive smoothing algorithm (Galis *et al.* 2010) to suppress the spurious high-frequency oscillations in the FE simulations.

For the ADER-DG simulations we select orders of accuracy $\mathcal{O}4$, $\mathcal{O}5$ and $\mathcal{O}6$, and edge length $h = 200$ m. Note that because the element size does not change, we can use the same mesh for all ADER-DG simulations.

The *x*-components of the slip rate at receivers R1 and R2 (Fig. 3) obtained with the square and the elliptical initiation zones are compared in Figs 4 and 5, respectively. The slip-rate curves are relatively simple due to the homogeneous configuration, but reveal a 2-step healing process: first, partial healing (at ~ 7 s at R1 and ~ 5 s at R2) occurs due to the healing pulse propagating from the longer edge of the fault while the second healing episode (at ~ 8 s) is caused by the healing pulse from the shorter edge of the fault.

Overall, the agreement between the ADER-DG and FE solutions for the square as well as the elliptical initiation zone is very good. However, zooming into the rupture times and peak amplitudes (inset
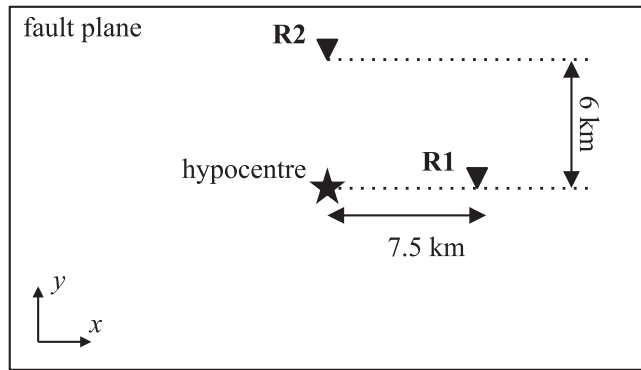
Figure 3. Positions of receivers R1 and R2 on the fault plane.

images in Figs 4 and 5) reveals differences in both the peak amplitudes and rupture times. In the following, we compare the 'less accurate' ADER-DG $\mathcal{O}4$ and FE $h = 100$ m solutions and the 'more accurate' ADER-DG $\mathcal{O}6$ and FE $h = 25$ m solutions in terms of difference in peak slip rate, $\Delta \dot{u}_{max}$, and difference in rupture time, ΔT_r. If methods produce consistent results, then difference between the ADER-DG and FE solutions should be decreasing with increasing accuracy. The results for the square and elliptical initiation zones are summarized in Table 2.

Examining differences in the peak slip rate, $\Delta \dot{u}_{max}$, in Table 2 we observe improvement in all cases except at receiver R2 for the square initiation zone. This is in accordance with our expectations, because the peak amplitudes in both methods vary non-monotonically with increasing accuracy, as shown in Figs 4 and 5. The explanation is different for the FE and ADER-DG methods. For the FE method, this is caused by the spurious high-frequency oscillations. The adaptive smoothing algorithm reduces the oscillations, but does not remove them completely. Moreover, the oscillations are stronger in the antiplane direction than in the in-plane direction. Therefore, the FE solutions at receiver R2 are more affected. The peak slip rates in the ADER-DG solutions, even though not affected by spurious high-frequency oscillations, exhibit slower convergence and relatively larger errors than the rupture time, as demonstrated by Pelties *et al.* (2012). The difference in rupture times, ΔT_r, in Table 2 provides more consistent results. The absolute value of ΔT_r decreases in all cases. Note that the change of sign of ΔT_r for the elliptical initiation zone may indicate different rupture speed in the FE and in ADER-DG simulations. However, ΔT_r for 'more accurate' results are very small and comparable with the time step used in the FE simulations ($\Delta t = 0.0024$ s for $h = 25$ m and $\Delta t = 0.0096$ s for $h = 100$ m), which indicates that the difference in rupture speed is not significant.

In addition to comparing the solutions obtained with both methods for the same initiation zone, it is also interesting to examine solutions obtained with one method for both initiation zones. The differences between the FE solutions obtained with varying element sizes are larger for the elliptical initiation zone than those for the square initiation zone (e.g. compare the rupture times of the FE solutions in Figs 4 and 5). This is likely a consequence of how well the initiation zone is represented by the mesh. The square initiation zone is exactly represented in meshes with all element sizes ($h = 25$, 50 as well as 100 m). On the other hand, the elliptical initiation zone is only approximately represented in the FE mesh. For $h = 100$ m the area of the effective initiation zone is 2.4 per cent smaller than area of the desired initiation zone, for $h = 25$ m the effective initiation zone is only 0.4 per cent smaller. On the other hand, if we compare the ADER-DG solutions obtained with different order of accuracy

$\mathcal{O}$ we observe smaller differences for the elliptical initiation zone (e.g. compare the rupture times of ADER-DG solutions in Figs 4 and 5). The increased accuracy, using higher-order basis functions, does not improve the representation of the initiation zone. This is true for both the square and elliptical initiation zones, which indicates that the observed differences in the ADER-DG solutions are not due to the mesh representation. We conjecture that ADER-DG will likely perform better for smooth configurations, as, for example the elliptical initiation zone. Therefore, the ADER-DG solutions converge faster for the elliptical initiation zone than for the square initiation zone.

Based on this analysis we conclude that the observed decrease of ΔT_r and $\Delta \dot{u}_{max}$, as well as overall very good agreement of all solutions demonstrate that both methods produce consistent results for square as well as elliptical initiation zones.

3.3 Effects of an incorrect size of the initiation zone

Here we illustrate that variations of the effective size (though small) may cause significant effects. For this purpose we perform the same tests with the square initiation zone as above. The desired size $2L_i = 1800$ m is an even multiple of the element size. Therefore, implementation (b) was used in the previous tests. Now we use implementation (a) that is appropriate if the size of the initiation zone is an odd multiple of the element size.

The results at receiver R1 are compared in Fig. 6. We observe that while implementation (a) leads to significant differences in rupture times, with the correct implementation (b) we can not distinguish the rupture times. There are also small differences in amplitude. The relative difference in amplitude between solutions obtained with implementations (a) and (b) are 2.2, 1.4 and 0.6 per cent for $h = 100$, $h = 50$ and $h = 25$ m, respectively. Larger amplitudes in the solutions obtained with the incorrect implementation (a) are likely a consequence of the larger effective size of the initiation zone. Due to the incorrect implementation the effective size of the initiation zone is not 1800 m but 1900 m for $h = 100$ m, 1850 m for $h = 50$ m and 1825 m for $h = 25$ m. The effect is even more important when examining relative dimensions of the initiation zone. For $h = 100$ m the effective initiation zone is only 5.6 per cent larger than the desired size, but the effects are significant. The effects are still very clear also for $h = 25$ m, when the initiation zone is only 1.4 per cent larger.

In absence of a reference analytical solution, the convergence rate of a method is an important parameter. Our numerical results indicate that the convergence rates of rupture time obtained with implementations (a) and (b) significantly differ. Consequently, the conclusions based on an analysis of the convergence of the rupture time might be misleading if effective size of the initiation zone is not taken into account.

3.4 Convergence of the critical size of the initiation zone

Understanding the sensitivity of the FE and ADER-DG methods to the shape of the initiation zone and its representation in the numerical mesh we now investigate the critical size of the initiation zone that leads to self-sustaining spontaneous rupture propagation.

For these tests we choose two extreme configurations, one with low strength parameter, $S = 0.1$, and one with high strength parameter, $S = 2.0$. Consequently, the initial tractions are $\tau_0 = 79.667$ and 69.111 MPa, respectively. We use the square initiation zone with the
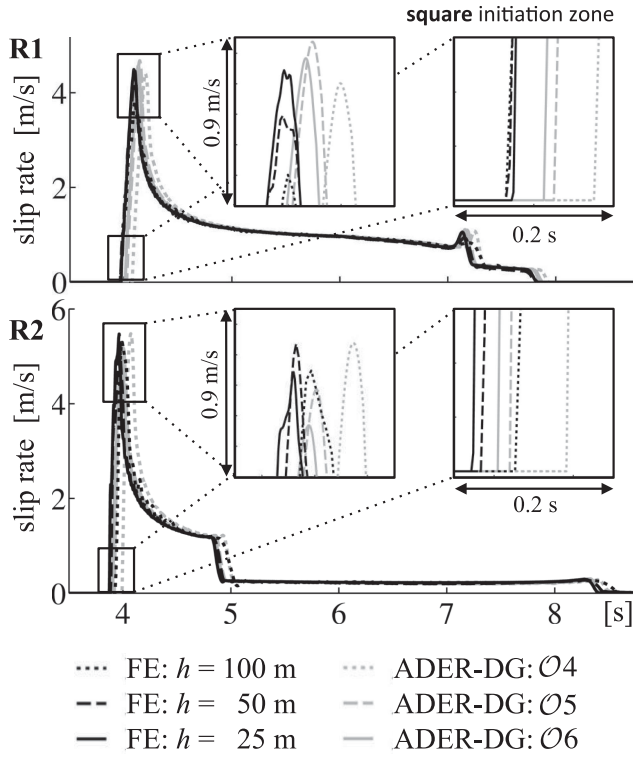
Figure 4. Comparison of the *x*-component of slip rate obtained with the FE and ADER-DG methods with different discretizations using the square initiation zone. Embedded images show details of peak amplitudes and rupture times.

Figure 5. Comparison of the *x*-component of slip rate obtained with the FE and ADER-DG methods with different discretizations using the elliptical initiation zone. Embedded images show details of peak amplitudes and rupture times.

initial tractions inside the initiation zone $\tau_0^i = 81.342$ and 81.394 MPa, respectively.

3.4.1 Convergence for the FE method

With the FE method we conduct the convergence test for $h = 200$, 150, 100, 75, 50, 37.5 and 25 m, and for $S = 2.0$ also $h = 18.75$ m (left-hand column of Fig. 7; $S = 0.1$ in the top and $S = 2.0$ in the bottom row; *x*-axis is the element size h). The effective half-length of the initiation zone, L_i, is always a multiple of $h/2$, therefore, the resolution of the size of the initiation zone depends on h. For example, $h = 200$ m allows simulations with $L_i = 600, 700, 800$, ... m and $h = 150$ m allows simulations with $L_i = 600, 675, 750$, ... m. For a better visual reference, the possible sizes of L_i for each element size are indicated in the figure by small dots. The unfilled symbols depict configurations in which the rupture did not spontaneously propagate and the filled symbols depict configurations with successful initiation.

We fit the numerical results for successful initiation with an exponential model $L_i = a \cdot e^{b \cdot h}$ depicted by the solid lines ($a = 733.5$,
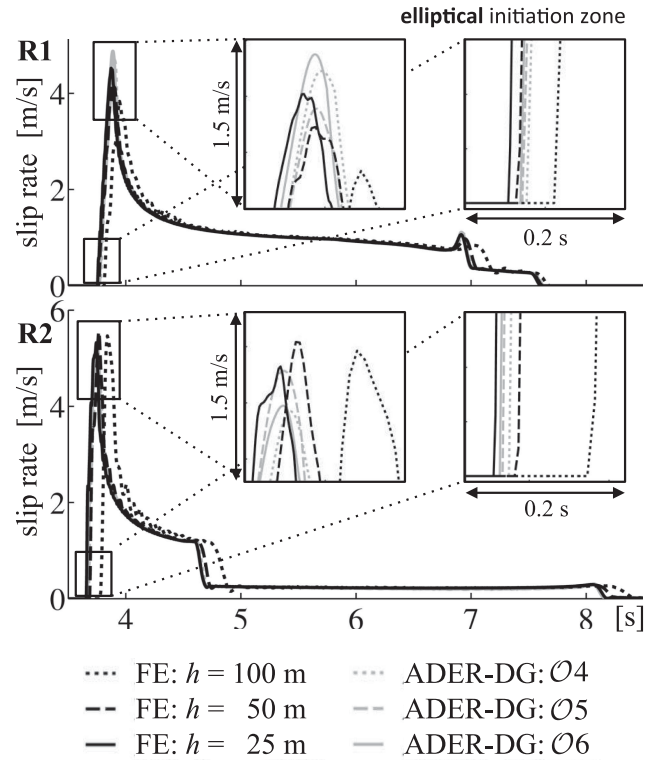
$b = 5.725 \times 10^{-4}$ and $a = 1380$, $b = 1.258 \times 10^{-4}$ for $S = 0.1$ and 2.0, respectively).

3.4.2 Convergence for the ADER-DG method

For convergence test of the ADER-DG method we use $\mathcal{O}3$, $\mathcal{O}4$ and $\mathcal{O}5$ accuracy with the element size $h = 300$ m, and $\mathcal{O}3$, $\mathcal{O}4$, $\mathcal{O}5$ and $\mathcal{O}6$ accuracy with element size $h = 200$ m. For $S = 2.0$ we also test $\mathcal{O}5$ accuracy with the element size $h = 100$ m. This mixture of different orders of accuracy and element sizes allows to reduce the number of simulations needed to determine the critical size. We analyse this set of simulations in terms of the parameter ν:

$$\nu = \frac{h}{\sqrt[3]{\text{dof}}}, \tag{5}$$

where dof is the number of degrees of freedom. For the ADER-DG method

$$\text{dof} = \frac{\mathcal{O} \cdot (\mathcal{O} + 1) \cdot (\mathcal{O} + 2)}{6}. \tag{6}$$

Since ADER-DG is applied on an unstructured tetrahedral mesh, prepared such that the elements honour the shape and size of the

Table 2. Quantitative comparison of the FE and AFER-DG solutions for square and elliptical initiation zones.

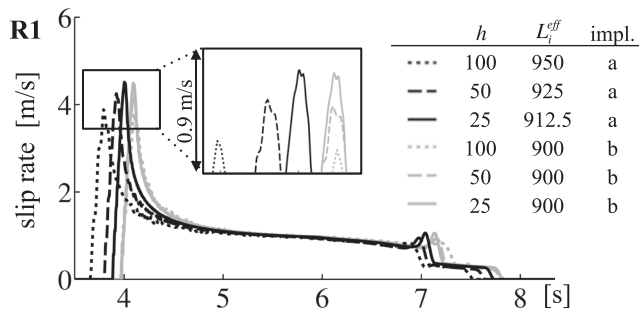|	Square initiation zone				Elliptical initiation zone			
	R1		R2		R1		R2	
	$\Delta \dot{u}_{\max}$	ΔT_r	$\Delta \dot{u}_{\max}$	ΔT_r	$\Delta \dot{u}_{\max}$	ΔT_r	$\Delta \dot{u}_{\max}$	ΔT_r
ADER-DG $\mathcal{O}4$ – FE $h = 100$ m	0.60	0.102	0.18	0.056	0.89	−0.044	−0.54	−0.107
ADER-DG $\mathcal{O}6$ – FE $h = 25$ m	0.08	0.039	−0.35	0.031	0.35	0.013	−0.35	0.005

Figure 6. Illustration of the effect of incorrect size of the initiation zone (for example, due to incorrect implementation of the square initiation zone in FE method). h is element size, L_i^{eff} is the effective half-length of the initiation zone and impl. indicate implementation (a) or (b), see Fig. 1. Note that the desired half-length of square initiation zone is 900 m.
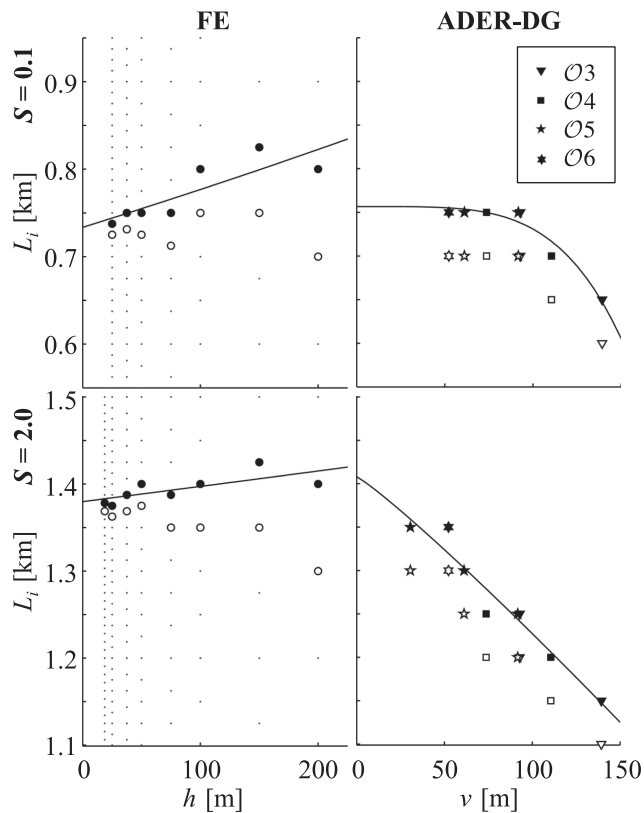

Figure 7. Convergence of the critical size of initiation zone using FE (left-hand side) and ADER-DG (right-hand side) methods. Filled symbols indicate successful initiation, unfilled symbols indicate unsuccessful initiation, small dots indicate numerically possible models in FE mesh. h is element size, $v = h / \sqrt[3]{\text{dof}}$.

initiation zone as precisely as possible, the elements inside and near the initiation zone may be very small. Therefore, it is generally possible to resolve very small changes in the initiation zone size. However, for efficiency reasons we fix the increments of the initiation zone variations to 50 m.

The convergence results for ADER-DG are shown in the right-hand column of Fig. 7. We fit the numerical results with a power law of the form $L_i = a \cdot v^b + c$, depicted by the solid lines ($a = -4.684 \times 10^{-8}$, $b = 4.369$, $c = 756.6$ and $a = -1.121$, $b = 1.104$, $c = 1408$ for $S = 0.1$ and 2.0, respectively).

3.4.3 Comparison and discussion of the FE and ADER-DG results

Our results in Fig. 7 indicate that the critical sizes of the initiation zone in the FE method converge to the same values as in the ADER-DG method. For the low-strength case, $S = 0.1$, our FE results show that the critical size of the initiation zone, L_i, converges to 734 m, while that of ADER-DG converges to 757 m. The small difference of only 23 m is below the chosen increment of the initiation zone size in the ADER-DG simulations (i.e. 50 m). Similarly, for the high-strength case, $S = 2.0$, the FE and ADER-DG results converge to 1380 and 1408 m, respectively. The difference is 28 m, again, below the chosen increment of the initiation zone size in the ADER-DG simulations. We therefore conclude that the critical sizes of the initiation zone converge in both methods to the same values.

Even though the convergence to the same critical size is the most important result, the convergence characteristics of the FE and ADER-DG methods are very different. The critical size from the FE simulations is slightly decreasing with decreasing h (i.e. with increasing accuracy). For example, for $S = 0.1$ and $L_i = 750$ m initiation was unsuccessful with the element size $h = 100$ m but was successful with element size $h = 75$ m. We conjecture that this behaviour is related to higher accuracy achieved with smaller elements. With finer spatial discretization the rupture-tip stress concentration is better resolved leading to narrower slip-rate peaks with larger amplitudes (as seen in Figs 4–6) and, consequently, a smaller initiation zone is sufficient for successful initiation.

There are two interesting features observed in the ADER-DG results: (i) very different convergence rates in the low- and high-strength cases and (ii) increase of the critical size with increasing accuracy. The critical size obtained by the ADER-DG method converges much faster for $S = 0.1$ than for $S = 2.0$ case. Our interpretation is that this is due to a step in the initial stress at the rim of the initiation zone (i.e. difference between τ_0^i inside the initiation zone and τ_0 outside). The difference is 1.7 and 12.3 MPa in the low ($S = 0.1$) and high ($S = 2.0$) strength cases, respectively. The high-order ADER-DG method is more sensitive to the abrupt change in the high-strength case than the low-order FE method. However, we do not have a conclusive explanation for the second observed feature. We expect that the observed behaviour is a consequence of joint influence of numerical artefacts, numerical dispersion, numerical diffusion and non-linear character of the initiation process.

4 THE CRITICAL SIZE OF THE INITIATION ZONE

It is useful to have an estimate of the critical size of the initiation zone for designing a dynamic-rupture simulation. However published estimates so far do not provide general rules for designing 3-D numerical simulations. In this section, we analyse the critical size for initiation zones of different shapes as a function of the strength parameter S, and compare our numerical results with published estimates of the critical size. The comparison motivates the derivation of new estimates.

4.1 Numerical simulations

We perform extensive numerical simulations to study the critical size of the square, circular and elliptical initiation zones (with the aspect ratio 4/3) for a range of the strength parameter S from 0.1 to 2.0. To obtain different strengths S, we consider various values of the initial traction and fixed μ_s, μ_d and τ_n (Table 1). The initial traction

inside the initiation zone was set as $\tau_0^i = \tau_s + 0.005 \cdot (\tau_s - \tau_0)$ (i.e. the overstress is 0.5 per cent of the strength excess).

We present the size of the initiation zone as a non-dimensional half-length,

$$L_{\text{init}} = L_i / L_{\text{fric}}, \tag{7}$$

or a non-dimensional area,

$$A_{\text{init}} = A_i / L_{\text{fric}}^2. \tag{8}$$

Here, $L_{\text{fric}} = \mu D_c / (\tau_s - \tau_d)$ is a characteristic length scale introduced by the slip-weakening process (e.g. Dunham 2007), L_i is the effective half-length of the initiation zone (side for square, radius for circular and a major semi-axis for elliptical initiation zone) and A_i is the effective area of the initiation zone.

Our main interest is to quantify the critical size of the initiation zone that leads to self-sustained rupture propagation. Therefore, we consider initiation successful if the rupture propagates over the whole fault plane. Otherwise the initiation is considered unsuccessful. Note that the area of the unsuccessfully initiated ruptures is significantly smaller than the total area of the fault. Consequently, our results are not biased by the finite fault size. For example, the slightly subcritical rupture for $S = 2.0$ with square initiation zone and $h = 100$ m ruptured less than 10 per cent of the entire fault area.

4.1.1 Numerical results for the critical half-lengths

Fig. 8 shows non-dimensional critical half-lengths for three considered shapes as a function of the strength parameter S. The half-lengths are obtained from numerical simulations for $h = 100$ m and $h = 50$ m. The shapes of the initiation zone are indicated by different symbols. Filled and unfilled symbols depict successful and unsuccessful initiation, respectively. We approximate the numerical results by a power law, $L_{\text{init}} = a \cdot S^b + c$, to simplify the comparison of the results for different element sizes as well as for different shapes of the initiation zone. Fig. 8 indicates that for a fixed S the critical half-length of the initiation zone is smallest for the square and largest for the elliptical initiation zone.
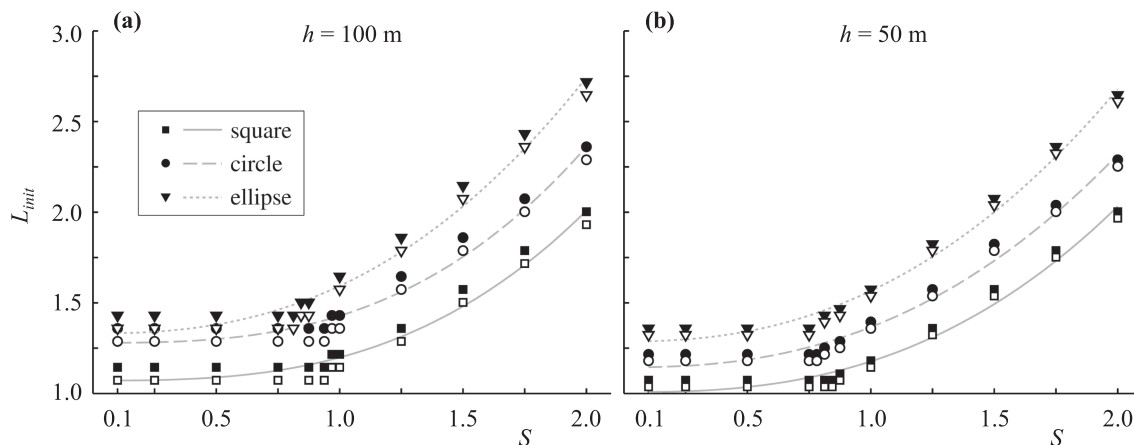
4.1.2 Numerical results for the critical area

Fig. 9 presents the same data as shown in Fig. 8, but in terms of the non-dimensional area. We again approximate the numerical results by a power law, $A_{\text{init}} = a \cdot S^b + c$. The results for $h = 50$ m indicate that the initiation area for the three considered shapes coalesce into a single power-law behaviour, depicted by the solid black line:

$$A_{\text{init}} = 1.75 \cdot S^{2.81} + 3.82. \tag{9}$$

The differences between the critical areas obtained with different shapes of the initiation zone visible in Fig. 9(b) are, in fact, expected considering the results of convergence of the critical half-length in the case of the square initiation zone.

4.1.3 The resolution of the half-length and area of the initiation zone

Interestingly, the S-dependence of the resolution of the initiation zone seems to change when results are presented as non-dimensional half-length and non-dimensional area (compare Figs 8 and 9). To explain this let us assume the square initiation zone in an FE mesh with element size h. The resolution of L_i is $h/2$ and it is independent of S (consequently, resolution of non-dimensional L_{init} is also independent of S). The area of the initiation zone with half-length L_i is $4 L_i^2$. Similarly, for half-length $L_i + h/2$ (where $h/2$ is the smallest increment of the half-length) we obtain area $4 (L_i + h/2)^2$. The resolution of the area of the initiation zone is the difference between these areas, that is, $4 (L_i + h/2)^2 - 4 L_i^2 = 4 h L_i + h^2$. We see that the resolution of the area depends on L_i, which depends on S, and consequently the resolution depends on S. Moreover, L_i is greater for larger S, leading to poorer resolution for larger S.

4.1.4 Discrete representation of the initiation zone

Comparing critical radii for lower S in Fig. 8 we observe significant change between $h = 100$ m and $h = 50$ m cases. However, we do not observe such change if results are presented as area (Fig. 9). This indicates that the larger radius only compensates poor representation of the circular shape in the mesh with $h = 100$ m and that the area of the initiation zone is less sensitive to imperfections in geometrical representation of the initiation zone due to numerical discretization.
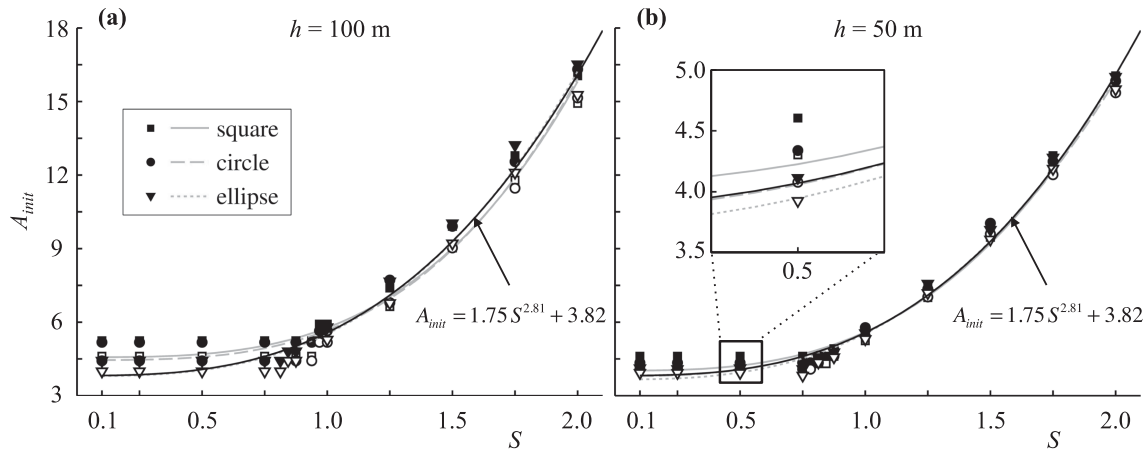
Figure 8. The non-dimensional critical length of the initiation zone L_{init} (eq. 7)—half-length for square, radius for circular and major semi-axis for elliptical initiation zone—as a function of non-dimensional strength parameter S (eq. 3). Comparison of numerical results obtained with element size $h = 100$ m (a) and $h = 50$ m (b). Filled symbols indicate successful and unfilled symbols indicate unsuccessful initiation. The shape of the initiation zone is indicated by different symbols. Numerical results were approximated by power laws indicated by grey lines.

Figure 9. The non-dimensional critical area A_{init} (eq. 8) of the square, circular and elliptical initiation zones as a function of non-dimensional strength parameter S (eq. 3). Comparison of numerical results obtained with element size $h = 100$ m (a) and $h = 50$ m (b). Filled symbols indicate successful and unfilled symbols indicate unsuccessful initiation. The shape of the initiation zone is indicated by different symbols. Numerical results are approximated by the power law, indicated by grey lines. Numerical results for $h = 50$ m and for all shapes of the initiation zone are also approximated by one power law depicted by black line (also plotted in (a) as a reference). Note that the approximate line for ellipse (dotted grey) coincides with the average line (solid black) for $h = 100$ m.

4.1.5 Implications

The previous discussion (in Sections 4.1.1, 4.1.2 and 4.1.4) and Figs 8 and 9 suggest that for a fixed overstress the initiation is not controlled by the half-length or shape, but rather by the area of the initiation zone. To confirm this hypothesis we consider two orientations of the elliptical initiation zone. In the first case, the major-semi axis points into the in-plane direction, reflecting the fact that in 2-D the critical half-length for the in-plane mode is greater than for the antiplane mode. In the second case, the major-semi axis points into the antiplane direction, and consequently, the half-length of the initiation zone is smaller in the in-plane direction than the critical half-length for the in-plane mode. For both orientations we consider an ellipse with the same aspect ratio. Simulations (for $S = 1.0$ only) provide exactly the same results for the critical area for both orientations, indicating that the half-length in the in-plane direction may be smaller than the critical half-length from 2-D models, as long as the initiation area is larger than the critical area. The numerical results thus support our hypothesis.

In the limit, if one axis of the overstressed asperity tends to infinity, the 3-D problem reduces to a 2-D problem, for which the criterion for runaway rupture involves a critical length. Hence, for very elongated initiation zones there is a critical length for the short axis, but not a critical area (Uenishi 2009). Our current results, including different shapes and aspect ratios of the overstressed asperity up to 4/3, show that the shape and aspect ratio have only a weak effect on the critical area if the aspect ratio is close to 1. However, we conjecture that also the effects of the aspect ratio could vary with S (e.g. similarly to the critical area depending on S). Because an initiation zone with aspect ratio close to 1 is important for most practical purposes, we leave it to future work to investigate in details the effects of the aspect ratio.

We also conjecture that our hypothesis does not apply for irregular shapes of the initiation zone. For instance, Ripperger *et al.* (2007) studied initiation with irregularly shaped initiation zones. Their results indicate that for successful initiation the radius of the inscribed circle of the initiation zone has to be greater than the 2-D antiplane critical half-length by Uenishi & Rice (2003) (see eq. 16).

Figs 8 and 9 also show that for $S \leq 0.75$ the critical size of the initiation zone appears to be independent of S, while for $S \geq 1.0$ it

increases with S. We will comment on this behaviour in more detail in Section 5.2.

4.2 Overview of existing theoretical estimates of the critical size of the initiation zone

Different estimates of the critical nucleation size have been derived for 2-D as well as 3-D problems using different assumptions. To simplify the later expressions we introduce the critical half-length (e.g. Day *et al.* 2005)

$$L_0 = \frac{\mu}{\pi} \frac{\tau_s - \tau_d}{(\tau_0 - \tau_d)^2} D_c \tag{10}$$

and weakening rate (e.g. Uenishi & Rice 2003)

$$W = \frac{\tau_s - \tau_d}{D_c}. \tag{11}$$

Andrews (1976a,b) determined the critical crack size in 2-D under the assumption of uniform stress drop, by deriving the half-length of a crack in static equilibrium that balances static energy release rate and fracture energy:

$$L_A^{II} = \frac{1}{1 - \nu} L_0 \tag{12}$$

and

$$L_A^{III} = L_0 \tag{13}$$

for mode II (in-plane) and mode III (antiplane), respectively. Following the same approach and again assuming uniform stress drop, Day (1982) derived the critical radius of a circular crack in 3-D, for a Poisson's ratio of 1/4,

$$L_D = \frac{7\pi^2}{24} L_0. \tag{14}$$

The estimates by Andrews (1976a,b) and Day (1982) differ only by a material-dependent factor but the dependency on S is the same (determined by L_0).

Uenishi & Rice (2003) determined the minimum half-length required to initiate dynamic rupture in 2-D by a gradually increasing and spatially concentrated stress load:

$$L_{U2}^{\mathrm{II}} \cong 0.579 \, \frac{1}{1-\nu} \frac{\mu}{W} \tag{15}$$

and

$$L_{U2}^{\mathrm{III}} \cong 0.579 \, \frac{\mu}{W} \tag{16}$$

for modes II and III, respectively. Subscript 2 indicates that estimates were derived for a 2-D problem. Uenishi (2009) extended the approach to 3-D and presented analytical formulas for the critical values of the major and minor semi-axes of an elliptical initiation zone aligned with the mode II and III directions, respectively:

$$L_{U3}^{a} \cong 0.624 \, C(\nu) \, \frac{1}{1-\nu} \frac{\mu}{W} \tag{17}$$

$$L_{U3}^{b} \cong 0.624 \, C(\nu) \, \frac{\mu}{W}. \tag{18}$$

Here

$$C(\nu) = \frac{E[\sqrt{\nu(2-\nu)}] + (1-\nu)K[\sqrt{\nu(2-\nu)}]}{2-\nu}, \tag{19}$$

where $K(k)$ and $E(k)$ are complete elliptic integrals of the first and second kind, respectively:

$$K(k) = \int_0^1 \frac{1}{\sqrt{(1-t^2)(1-k^2 t^2)}} \, dt, \tag{20}$$

$$E(k) = \int_0^1 \sqrt{\frac{1-k^2 t^2}{(1-t^2)}} \, dt. \tag{21}$$

These formulas are valid for a particular value of the aspect ratio of the critical zone, $a/b = 1/(1-\nu)$. Uenishi (2009) presented numerical results of critical lengths for a wide range of values of the aspect ratios and Poisson's ratio $\nu = 0.25$.

Note that estimates by Andrews (1976a,b) and Day (1982) depend on the initial traction τ_0, whereas estimates by Uenishi & Rice (2003) and Uenishi (2009) do not depend on the background initial traction τ_0. This is likely a consequence of the assumptions used to derive the critical half-lengths. Andrews and Day assumed a pre-existing crack with uniform initial stress and a breakdown zone small compared with the crack size, while Uenishi & Rice (2003) and Uenishi (2009) included gradual loading of the fault with a corresponding aseismic slip, non-uniform initial stress and a breakdown zone occupying the whole crack. More importantly, they did not address the question of whether or not the rupture becomes indefinitely self-sustained after initiation. Their critical size for rupture initiation does not necessarily imply a critical size for a runaway rupture (e.g. Viesca & Rice 2012) but does provide a lower bound for it. None of the situations treated by these authors completely matches the overstressed-asperity initiation procedure considered here. Next, we compare their critical size estimates with results of numerical simulations.

4.3 Comparison of the numerical results with the theoretical estimates

Our numerical results indicate that the critical area does not depend on the shape of the initiation zone. Therefore, it is natural to choose the critical area to compare the theoretical estimates with the numerical results. It is straightforward to obtain the critical area for

estimates based on analysis of a 3-D problem because the shape of the initiation zone is explicitly assumed. However, for 2-D estimates we have to assume a shape. Different critical lengths for modes II and III, derived using the same approach, naturally suggest an elliptical shape. Having only circular (Day's estimate) and elliptical (all other estimates) shapes we can define a general formula for the total area of the initiation zone in the following form:

$$A_c = \pi L_c^a L_c^b. \tag{22}$$

The precise definitions of L_c^a and L_c^b change according to the considered estimate. Day (1982) assumed a circular crack and consequently $L_c^a = L_c^b = L_D$. Uenishi (2009) considered an elliptical initiation zone and naturally $L_c^a = L_{U3}^a$ and $L_c^b = L_{U3}^b$. Considering the approach used for obtaining estimates for modes II and III, we can combine (a) the estimate by Andrews (1976a) with that by Andrews (1976b) and obtain $L_c^a = L_A^{\mathrm{II}}$ and $L_c^b = L_A^{\mathrm{III}}$; (b) the estimates by Uenishi & Rice (2003) and obtain $L_c^a = L_{U2}^{\mathrm{II}}$ and $L_c^b = L_{U2}^{\mathrm{III}}$.

Comparing the non-dimensional estimates of critical area with our numerical results in Fig. 10(a) we find that none of these estimates is consistent with our findings over the entire S-range considered. The critical area obtained from our numerical simulations increases with S, whereas the estimates by Uenishi & Rice (2003) and Uenishi (2009) are S-independent. Even though the critical area predicted by estimates by Day (1982) and Andrews (1976a,b) increases with S, we observe significant differences compared with our numerical results. Moreover, comparing eqs (12), (13) and (14), we find that the estimates by Andrews and Day differ only by a (material dependent) multiplicative factor whereas the dependence on S is determined by L_0, eq. (10). Consequently, the corresponding critical areas are proportional to the critical area for a circular crack with radius L_0, that is, $A_c \sim \pi L_0^2$. Comparison with numerical results suggests that introduction of another multiplicative factor to πL_0^2 will not lead to sufficient agreement with our numerical results.

Although none of the estimates is consistent with our numerical results over the entire S-range considered in this study, Fig. 10(a) shows very good agreement of the estimate by Uenishi (2009) with our results for $S \lesssim 0.75$. In fact, if we look at the detail in the zoomed-in image, we see that the estimate is in excellent agreement with numerical results for the elliptical shape. (The differences between square, circular and elliptical shapes are due to different convergence characteristics.) The consistency of this estimate with numerical results for low S is expected. The theory predicts the minimum size of an overstressed asperity that allows for initial rupture acceleration, regardless of what happens to the rupture later. However, if the background stress is high enough (S is low enough) the available elastic energy is sufficient for the initial acceleration to induce a runaway rupture. On the other hand, if the background stress is low (S is high) the near critical ruptures stop spontaneously at a distance much larger than the process zone size, and the problem becomes closer to one that can be idealized in the context of small-scale yielding.

Because none of the theoretical estimates sufficiently agrees with our numerical results for the high-strength configurations, we derive a new estimate for the nucleation area. We develop two new theoretical estimates (see Appendix A) for the high-strength configurations

$$A_1 = \frac{(3\pi)^3}{2^{11}} \frac{\tau_0 - \tau_d}{\tau_0^i - \tau_0} \frac{(\tau_s - \tau_d)^2}{(\tau_0 - \tau_d)^4} \mu^2 D_c^2 \tag{23}$$
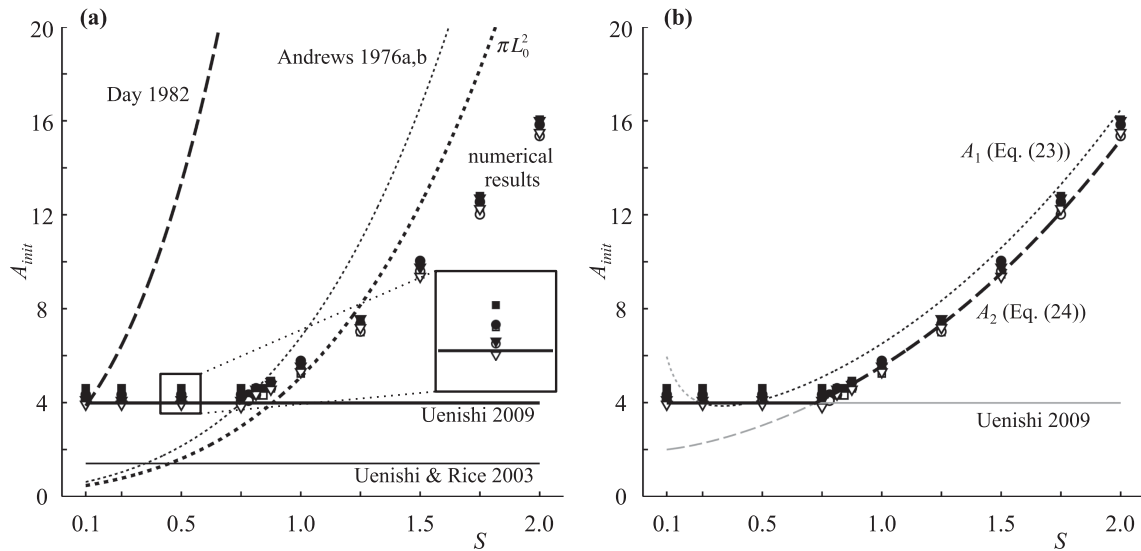
Figure 10. Comparison of theoretical estimates of the non-dimensional critical area A_{init} (eq. 8) as a function of the non-dimensional strength parameter S (eq. 3) with our numerical results (for element size $h = 50$ m; depicted by symbols as used in Fig. 9). (a) Comparison with previous estimates. Note that estimates based on analysis of a 3-D problem are shown by thick lines while estimates based on analysis of a 2-D problem are shown by thin lines. (b) Comparison with estimates consistent with numerical results—our new estimates, A_1 (eq. 23) and A_2 (eq. 24), and estimates by Uenishi (2009). The range of validity for each estimate is indicated by black thick lines.

and

$$A_2 = \frac{\pi^3}{16} \frac{1}{f_{\min}^4} \frac{(\tau_s - \tau_d)^2}{(\tau_0 - \tau_d)^4} \mu^2 D_c^2, \tag{24}$$

where $f_{\min}$ in eq. (24) is a minimum of the function

$$f(x) = \sqrt{x} \left[1 + \frac{\tau_0^i - \tau_0}{\tau_0 - \tau_d} \left(1 - \sqrt{1 - 1/x^2} \right) \right]. \tag{25}$$

Deriving $f_{\min}$ analytically does not seem to yield a compact expression, therefore we evaluate it by numerical minimization.

Fig. 10(b) shows even better agreement between both our new estimates and the numerical results, compared with other theoretical estimates shown in Fig. 10(a). The advantage of estimate A_1 is its compact analytical expression, however, it can be used only as an approximation to estimate A_2. On the other hand, even though estimate A_2 has a more complex form, it is based on more complete theoretical basis and its agreement with our numerical results for $S \gtrsim 0.75$ is excellent. Thus, we conclude that the most rigorous theoretical estimate for the whole S range is

$$A_C = \max(A_U, A_2) \tag{26}$$

where A_U is critical area estimated following Uenishi (2009), that is, using eqs (17), (18) and (22). In principle, we can determine the point where A_C changes from A_U to A_2 by solving the equation $A_U = A_2$. However, because $f_{\min}$ implicitly depends on S, the equation does not have an analytical solution. Solving $A_U = A_2$ numerically yields $S \cong 0.72$. Note that, if we rewrite eqs (23) and (24) in terms of fracture energy G_c, the estimates A_1 and A_2 apply to any friction law with finite fracture energy only if the rupture is crack-like because assumption (iii) in Appendix A is not valid for pulse-like ruptures. However, Uenishi's estimates are valid only for linear slip-weakening friction (Rice & Uenishi 2010).

5 THE EFFECT OF OVERSTRESS INSIDE THE INITIATION ZONE

We now turn to a detailed analysis of overstress in the initiation zone. In the previous section we examined the critical area for a fixed, very small overstress. Intuitively, a smaller overstress could lead to a larger critical area and a larger overstress could lead to a smaller critical area. Therefore, we examine how the overstress affects the critical area and analyse its effects on subsequent rupture propagation.

5.1 Critical area assuming overstress smaller than $0.005 \cdot \Delta\tau_E$

In Section 4, we assessed the critical size of the initiation zone assuming the fixed overstress of 0.5 per cent of the strength excess (i.e. $\Delta\tau_0 = 0.005 \cdot \Delta\tau_E$). The strength excess increases with increasing S (as a consequence of fixed τ_s and τ_d). Therefore, the evaluated overstress (in Pa) also increases with increasing S. In particular, the overstress is 8 333 and 61 111 Pa for $S = 0.1$ and 2.0, respectively. We perform numerical simulations with the fixed overstress $\Delta\tau_0 = 50$ Pa to examine whether application of a smaller overstress leads to a larger critical area. We perform simulations only using the square initiation zone and the baseline grid spacing, that is, $h = 100$ m.

As shown in Fig. 11, both levels of overstress lead to the same critical area for five considered S values. Fig. 11 also shows that critical areas estimated by A_1 and A_2 (we do not include the estimate by Uenishi (2009) in this comparison because it does not include the overstress) for both levels of overstress are nearly indistinguishable (relative difference of the critical area for $S = 2.0$ is only 0.5 per cent). Thus, both the numerical results and the theoretical estimates indicate that the overstress 0.5 per cent of the strength excess is small enough, while smaller values do not lead to a significantly larger initiation area.
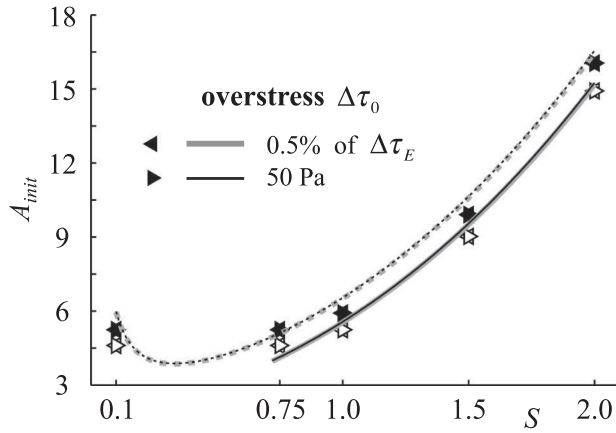
Figure 11. Comparison of non-dimensional critical area A_{init} (eq. 8) as a function of the non-dimensional strength parameter S (eq. 3) obtained from numerical simulations for overstress 0.5 per cent of strength excess (indicated by left-pointing triangles) and 50 Pa (indicated by right-pointing triangles). Filled symbols indicate successful and unfilled symbols indicate unsuccessful initiation. The left- and right-pointing triangles at the same position form a hexagram. Numerical results are also compared with the estimates A_1 (dashed line) and A_2 (solid line). Note that we do not include the estimate by Uenishi (2009) in this comparison because it does not include the overstress.

5.2 Critical area assuming overstress larger than $0.005 \cdot \Delta\tau_E$

To examine how larger overstress affects the critical area of the initiation zone we assume a smaller initiation area and search for values of critical overstress that still lead to sustained dynamic rupture. We progressively change the area of the initiation zone as allowed by the mesh, starting with the area obtained for overstress $0.005 \cdot \Delta\tau_E$. For each area we gradually increase the overstress until we observe successful initiation. For efficiency reasons we fix the increments of the overstress to $0.05 \cdot \Delta\tau_E$, that is, 5 per cent of the strength excess. We again choose to perform simulations only using the square initiation zone and the baseline grid spacing, that is, $h = 100$ m.

Symbols in Fig. 12 show how the critical overstress varies with the initiation area. Different symbols represent five considered values of the strength parameter. These numerical results suggest that

for achieving successful initiation a smaller initiation area may be compensated by a larger overstress.

For low S values (0.1 and 0.5) and small overstress values (say, below 50 per cent of $\Delta\tau_E$) the critical area hardly depends on S. This is consistent with our findings in Fig. 10, but we further observe here that the minimum critical area depends on the amount of overstress. For larger overstress values, the critical area depends appreciably on S (as indicated by differences between $S = 0.1$ and 0.5 solutions for larger overstress, say, above 50 per cent of $\Delta\tau_E$). Consequently, the critical area for larger overstress depends on S in the entire S-range considered here.

Even though differences between the critical overstresses are small, compared with differences between the areas for $S = 0.5$ and 1.0, they increase with decreasing initiation area. This behaviour indicates that in the limit of no overstress the critical area for $S = 0.1$ is the same as for $S = 0.5$ and the critical area for $0.005 \cdot \Delta\tau_E$ and $S \lesssim 0.75$ (Fig. 9) varies with S, but its variation is too small to be captured by the $h = 50$ m elements. In fact, considering the differences between the areas for $S = 0.1$ and 0.5 shown in Fig. 12 we expect that the variations are negligible.

In addition to these numerical results we also analyse estimates of the critical overstress given by A_1 and A_2. For the estimate A_1 it is straightforward to derive an expression for τ_0^i and for the critical overstress $\Delta\tau_0$ as a function of the critical area, A:

$$\Delta\tau_0 = \frac{(3\pi)^3}{2^{11}} \frac{\tau_0 - \tau_d}{A} \frac{(\tau_s - \tau_d)^2}{(\tau_0 - \tau_d)^4} \mu^2 D_c^2 + \tau_0 - \tau_s. \qquad (27)$$

However, such an approach is not applicable for A_2 because it does not have analytical form. Therefore, we insert the critical overstress obtained from numerical results into eq. (24) to obtain an estimate of the critical area.

For $S \geq 1.0$, Fig. 12 indicates good agreement of the critical overstress obtained using estimates A_1 and A_2 (depicted by lines) with our numerical results. Estimates A_1 are plotted for $S \geq 0.5$ and estimates A_2 for $S \geq 1.0$, in agreement with validity ranges observed in Section 4. The agreement of estimate A_1 is good for $S \geq 1.0$, but for $S = 0.5$ the agreement is rather poor. We thus conclude that estimate A_1 should not be used for $S \lesssim 0.75$ if $\Delta\tau_0 > 0.005 \cdot \Delta\tau_E$. Although the agreement between estimate A_2 and our numerical results decreases with increasing overstress, the agreement is better than that for estimate A_1.

Although a theoretical estimate of the critical area for $S \leq 0.75$ as a function of overstress is not attempted here, note that for $S \leq 0.75$
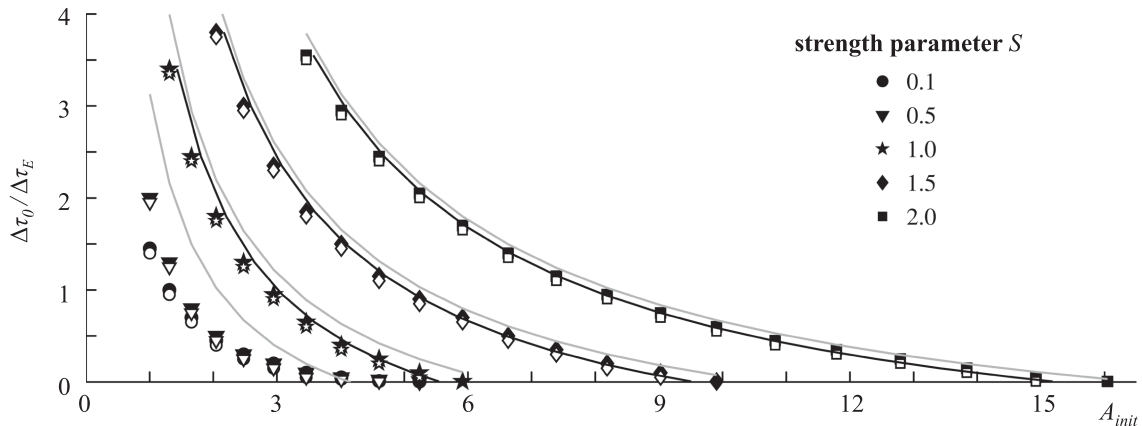

Figure 12. The critical overstress $\Delta\tau_0$ normalized by the strength excess $\Delta\tau_E$ as a function of non-dimensional area of initiation zone, A_{init}. Numerical simulations were performed for five values of strength parameter S, as indicated by different symbols. Filled symbols indicates successful initiation while unfilled symbols indicates unsuccessful initiation. The numerical results are compared with the estimates A_1 (grey lines) and A_2 (black lines).

the critical area from numerical simulations with higher overstress is systematically smaller than the estimate by Uenishi (2009). Results presented by Bizzarri (2010) for $S = 0.4$ and $\Delta\tau_0/\Delta\tau_E = 0.0546$ indicate a critical area of $1.45^2 \cdot \pi \cdot L_A^{II} \cdot L_A^{III}$, significantly smaller than A_U. This is consistent with the decrease of critical area as a function of increasing overstress shown in Fig. 12.

We also note that Bizzarri (2010) unfortunately did not correctly present results of Galis *et al.* (2010) who determined a critical major semi-axis length of $1.36 \cdot L_A^{II}$ for an elliptical initiation zone when $S = 0.5$. Although they made no generalization to other S values, Bizzarri (2010) interpreted their results as suggesting a critical length valid for supershear ruptures in general. He found his interpretation to be challenged by the critical length of $1.45 \cdot L_A^{II}$ he determined for $S = 0.4$. Here we found that the critical size is not proportional to Andrews' length L_A^{II} but, for supershear ruptures with $S \lesssim 0.75$, it is close to the S-independent length L_{U3}^a. The critical lengths of $1.36 \cdot L_A^{II}$ for $S = 0.5$ (Galis *et al.* 2010) and $1.45 \cdot L_A^{II}$ for $S = 0.4$ (Bizzarri 2010) are not in contradiction; both are actually consistent with the results of the present study and consistent with Uenishi's (2009) theory at low overstress.

Our numerical results as well as theoretical estimates indicate that for successful initiation the larger overstress may compensate smaller initiation area. However, a detailed analysis of the effects of higher overstress with smaller initiation area on the dynamic rupture evolution is necessary for practical applications.

5.3 Effects of initiation by a smaller area and higher overstress on rupture propagation

Section 5.2 shows that for the successful initiation with an initiation area smaller than that for $\Delta\tau_0 = 0.005 \cdot \Delta\tau_E$ one can use a higher overstress. This may be useful for practical applications, for example, it may allow initiation with smaller initiation zone in high-strength configurations, where a critical size for small overstress tends to be very large. However, before drawing such a conclusion, it is necessary to verify the effects of such an initiation on the subsequent rupture propagation.

First, we examine effects caused by increasing overstress from $0.005 \cdot \Delta\tau_E$ to $0.05 \cdot \Delta\tau_E$, because in the worst case, the critical overstress obtained from the numerical simulations (Fig. 12) may be almost $0.05 \cdot \Delta\tau_E$ larger than the minimum required overstress for a given initiation area. We consider only two limiting cases, with the strength parameter $S = 0.1$ and $S = 2.0$, and analyse rupture time, rupture speed, slip rate and traction. Our analysis (Appendix B) shows only negligible differences for $S = 0.1$. The level of agreement for $S = 2.0$ is also acceptable, however, the comparison reveals notable differences, particularly in rupture speed at smaller distances from the hypocentre. The results thus confirm that the increased overstress (in the considered range) does not significantly affect the solutions.

Taking our previous results into account we analyse the effects of higher overstress scaled according to the chosen initiation area by examining rupture time, rupture speed, slip rate and traction for the low-strength ($S = 0.1$) and high-strength ($S = 2.0$) configurations. For each configuration we consider four values of overstress. For each value of overstress we perform two simulations: (1) 'slightly overcritical'—with the initiation area barely larger than the critical area for considered overstress, that is determined according to results in Fig. 12; (2) 'supercritical'—with the initiation area corresponding to small overstress, that is, determined according to results in Fig. 9.

The detailed analysis (Appendix C) shows that the slightly overcritical initiation does not have essential effects on rupture propagation, even if the overstress is rather large. The analysis for the low-strength configuration shows small differences in rupture speed near the initiation zone. However, for the high-strength configuration we observe stronger effects. For the supercritical case we observe a supershear transition, significantly larger peak slip-rate amplitudes as well as significant changes in shape and amplitude of the stress variation caused by the hypocentral S wave. Yet, if we set the initiation area equal to the critical value for the (higher) overstress we observe different rupture speed only in the vicinity of the initiation zone, while differences in shape and amplitude of the stress variation caused by the hypocentral S wave are also significantly smaller.

Therefore, our results suggest that the initiation area and overstress close to their critical values do not lead to strong artefacts, even if the overstress is large.

6 DURATION OF THE INITIATION

The initiation of rupture propagation by an overstressed asperity is not an instantaneous process. Although the overstress causes immediate non-zero slip-rate inside the initiation zone, building-up sufficient stress for rupture to propagate outside its initiation zone takes some time. Moreover, the initiation has to be sufficiently strong for supporting rupture to propagate far enough to become fully spontaneous. From rupture initiation until its fully spontaneous propagation, the dynamic process is controlled by the artificial initiation. Because we are typically interested in earthquake dynamics it is useful to minimize duration of the initiation to make numerical simulations more efficient. This can be achieved by either a higher overstress or a larger initiation area. However, if they are too large they can affect resulting self-sustained dynamic rupture. Therefore, we examine relations between the initiation area, overstress and duration of the initiation in order to find optimal parameters.

The duration of the initiation can be defined as time from the beginning of the simulation until the moment when rupture propagation is no longer controlled by the initiation procedure. However, it is not straightforward to unambiguously define this instant in time, and consequently it is complicated to define the duration of the initiation in the absolute sense. On the other hand, a difference in the rupture times of two solutions for different initiation parameterizations at a location far enough from the hypocentre can be attributed to differences in the duration of the initiation. Thus, differences in the rupture times in our numerical simulations can be considered a relative measure of the initiation duration with respect to a reference solution. We define the relative difference in the rupture time as

$$\Delta T_r = \frac{T_r - T_r^{ref}}{T_{prop}} \times 100, \tag{28}$$

where T_r is the rupture time (i.e. the time when slip rate first time exceeds 1 mm s^{-1}) 10 km $\approx 14.3 \cdot L_{fric}$ away from the hypocentre in the in-plane direction, T_r^{ref} is the corresponding reference rupture time and T_{prop} is the time the rupture needs to reach the fault boundary in the in-plane direction. We use $T_{prop} = 3.5$ s for $S = 0.1$ and $T_{prop} = 9$ s for $S = 2.0$. We quantitatively compare the effects of a larger initiation zone or overstress using relative difference in peak slip rate,

$$\Delta\dot{u}_{max} = \frac{\dot{u}_{max} - \dot{u}_{max}^{ref}}{\dot{u}_{max}^{ref}} \times 100, \tag{29}$$
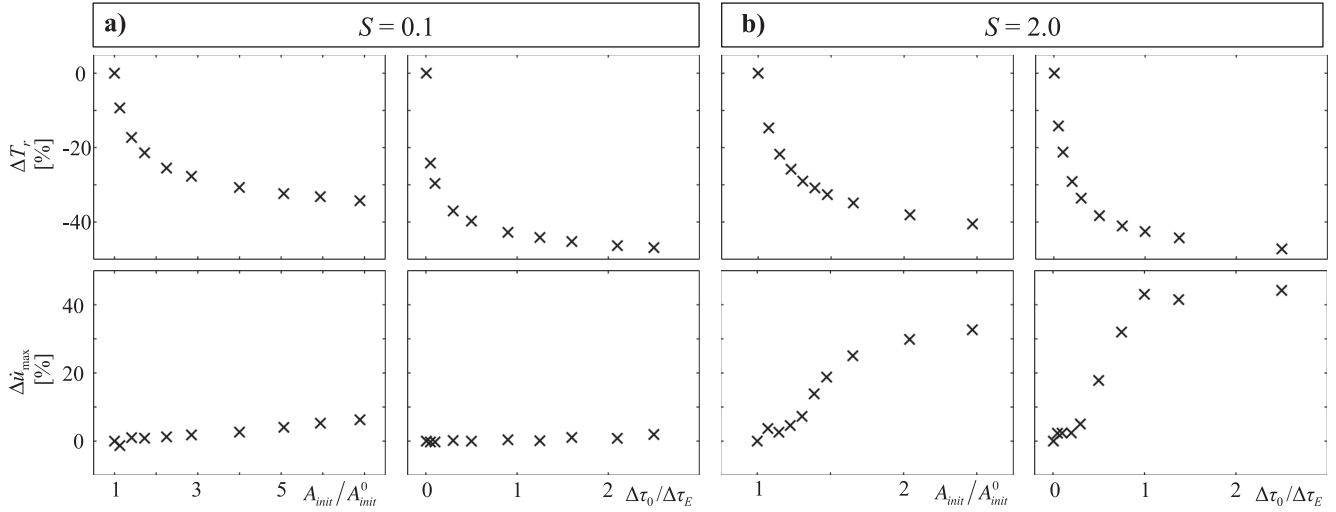
Figure 13. Illustration of effects of size of the initiation zone and overstress on the duration of the initiation and peak slip rate amplitude for low-strength configuration (a) and high-strength configuration (b). ΔT_r is the relative difference in rupture time with respect to reference solution, $\Delta \dot{u}_{\max}$ is the relative difference in peak slip rate with respect to the reference solution.

where $\dot{u}_{\max}$ is the peak slip rate at the same location as specified above and $\dot{u}_{\max}^{\mathrm{ref}}$ is the peak slip rate of the reference solution.

To analyse effects of the larger initiation area and overstress separately, we consider (i) several values of the initiation area with the fixed overstress $\Delta\tau_0 = 0.005 \cdot \Delta\tau_E$ and (ii) several values of the overstress with the fixed initiation area A_{init}^0, that is, the critical area for overstress $\Delta\tau_0 = 0.005 \cdot \Delta\tau_E$. We again consider the low-strength ($S = 0.1$) and high-strength ($S = 2.0$) configurations, square initiation zone and baseline element size $h = 100$ m. According to our definition of the numerical artefacts, we choose solutions obtained with the smallest initiation area, A_{init}^0, and the smallest overstress, $\Delta\tau_0 = 0.005 \cdot \Delta\tau_E$ as reference solutions. Here we present a quantitative summary of the results while detailed comparisons (including rupture time, rupture speed, slip rate and traction) of the six solutions from each set are presented in Appendix D.

For the low-strength configurations (Fig. 13a) we observe that although a larger initiation area may be used to shorten the duration of the initiation, application of a higher overstress leads to shorter duration and to smaller artefacts. As indicated in Appendix D, an initiation area larger than $2 \times A_{\mathrm{init}}^0$ leads to significant changes of rupture shape. At the same time, it does not lead to additionally shortened duration. On the other hand, we observe that application of the higher overstress does not only lead to better relative speed-up, compared with using a larger initiation area, but also to significantly smaller $\Delta \dot{u}_{\max}$. Moreover, we do not observe changes in rupture shape. Fig. 13(a) shows that ΔT_r saturates for $\Delta\tau_0/\Delta\tau_E > 1.0$, that is, the higher overstress does not lead to further shortening of the duration. Therefore, our analysis for the lower-strength configurations suggests that the overstress up to $\Delta\tau_0/\Delta\tau_E = 1.0$ efficiently shortens the duration of the initiation without introducing artefacts in subsequent rupture propagation.

For the high-strength configurations we find that applying a larger initiation area to achieve shorter initiation duration is preferable. Fig. 13(b) reveals strong gradients in $\Delta \dot{u}_{\max}$ for the larger initiation area and overstress. Considering $\Delta \dot{u}_{\max} \lesssim 5$ per cent a reasonably small error we find that we can use an initiation area $A_{\mathrm{init}} \lesssim 1.2 \times A_{\mathrm{init}}^0$ or overstress $\Delta\tau_0/\Delta\tau_E \lesssim 0.3$. While the detailed analysis (Appendix D) indicates that the larger initiation area or the larger overstress within these limits lead to comparably small artefacts, the larger overstress leads to more pronounced shortening of the

duration than the larger initiation area. However, taking into account the strong gradient in $\Delta \dot{u}_{\max}$ for $\Delta\tau_0/\Delta\tau_E > 0.3$, we conclude that for the higher-strength configurations it is preferable to apply the larger initiation area, up to $A_{\mathrm{init}} \sim 1.2 \times A_{\mathrm{init}}^0$, to efficiently shorten the duration of the initiation without affecting spontaneous rupture propagation.

For an elliptical initiation zone with the aspect ratio $1/(1 - \nu)$ Bizzarri (2010) found that a major semi-axis length equal to L_D by Day (1982) leads to results closest to those obtained with the forced-rupture initiation procedure for $S = 0.4$ and 2. He defined the length as the 'optimal' initiation length. In contrast, in our definition the optimal length minimizes initiation duration while preserving similarity to slightly overcritical ruptures. Bizzarri's (2010) optimal area, $\pi \cdot L_D^2/(1 - \nu)$, is significantly larger than the critical area for self-sustained rupture, as seen in Fig. 10, and generally larger than our optimal area.

7 CONCLUSIONS

We performed an extensive parametric study to estimate critical and optimal parameters of the initiation zone in spontaneous dynamic rupture simulations using a linear slip-weakening friction law and the overstressed-asperity initiation procedure.

Solutions obtained with the FE and ADER-DG methods for the square and elliptical initiation zones are in good agreement. The critical size of the initiation zone obtained from the FE simulations and that obtained from the ADER-DG simulations converge to the same value. Both methods thus provide consistent results. Subsequently, we applied the computationally more efficient FE method to perform extensive numerical simulations for this parametric study.

We found that the area, not the half-length, of the initiation zone controls the initiation of spontaneous rupture propagation in 3-D. Our findings indicate that a particular shape of the initiation zone is less important if its aspect ratio is ~ 1. However, in the limit of infinite aspect ratio the 3-D problem reduces to 2-D problem, for which nucleation is then controlled by a critical half-length. For successful initiation with irregularly shaped initiation zones, as indicated by Ripperger *et al.* (2007), a radius of a circle inscribed in

the initiation zone has to be larger than the critical half-length for mode III by Uenishi & Rice (2003).

Our numerical results indicate that for $S \lesssim 0.75$ the critical area is either independent of S or varies only marginally but the finite resolution of our simulations does not allow distinguishing the two cases. In this range of S and for a small overstress (e.g. $\Delta\tau_0 = 0.005 \cdot \Delta\tau_E$), the estimate by Uenishi (2009), eqs (17)–(22), may be used for assessing the critical area of the initiation zone. Since none of the previously published estimates seem to be applicable for $S > 0.75$, we propose a new estimate, A_2, eqs (24) and (25), which is in very good agreement with our numerical results for $S \in [0.75, 2.0]$, including larger overstress values.

Simulations with different overstress show that there is no difference in critical area for very small overstress ($\Delta\tau_0 = 50$ MPa or $\Delta\tau_0 = 0.005 \cdot \Delta\tau_E$), and that a larger overstress leads to a smaller critical area. For a fixed initiation area, larger overstress values may lead to strong numerical artefacts (e.g. changes of rupture shape and speed, artificial supershear transition, higher slip-rate amplitudes), particularly if S is large. However, if the overstress is set close to the critical value corresponding to the initiation area, the numerical artefacts are minimized. This could be useful in cases when the critical area for a small overstress is very large. Estimates A_1 and A_2 may be used to determine the critical area for larger overstress. Estimate A_1 may be also used to determine the critical overstress for given initiation area.

Our analysis of initiation duration suggests that overstress $\Delta\tau_0 \lesssim \Delta\tau_E$ may efficiently shorten the duration of the initiation in the low-strength configurations without introducing artefacts. For higher-strength configurations, a larger initiation area $A_{\mathrm{init}} \lesssim 1.25 \times A_{\mathrm{init}}^0$ leads to better results.

Our results provide general guidelines for proper and efficient initiation of spontaneous rupture propagation. Beyond its significance for computational earthquake dynamics, the fundamental understanding of the conditions that enable self-sustained (also called runaway) ruptures near an overstressed asperity can contribute to the quantitative assessment of failure and hazard in a range of contexts that involve loading by a concentrated stress. These include the nucleation of earthquakes and foreshocks driven by stress concentration near the boundaries between creeping and locked fault areas, for example at the base of the seismogenic zone; the initiation of frictional sliding near point loads in laboratory experiments (Rubinstein *et al.* 2007; Kammer *et al.* 2014); induced seismicity near concentrated loads generated by fluid injection (Garagash & Germanovich 2012), and the initiation of landslides by locally elevated pore pressures (Viesca & Rice 2012). The overstressed asperity initiation is admittedly a crude representation of these situations, but it encapsulates some of their key physical ingredients and hence is a basic model that can provide insight into more realistic situations, as illustrated by the work of Ampuero *et al.* (2006) and Ripperger *et al.* (2007).

ACKNOWLEDGEMENTS

REFERENCES

Ampuero, J.-P. & Ben-Zion, Y., 2008. Cracks, pulses and macroscopic asymmetry of dynamic rupture on a bimaterial interface with velocity-weakening friction, *Geophys. J. Int.,* **173**(2), 674–692.

Ampuero, J.-P. & Rubin, A.M., 2008. Earthquake nucleation on rate-and-state faults: aging and slip laws, *J. geophys. Res.,* **113,** B01302, doi:10.1029/2007JB005082.

Ampuero, J.-P., Vilotte, J.-P. & Sïnchez-Sesma, F.-J., 2002. Nucleation of rupture under slip dependent friction law: simple models of fault zone, *J. geophys. Res.,* **107**(B12), 2324, doi:10.1029/2001JB000452.

Ampuero, J.-P., Ripperger, J. & Mai, P.M., 2006. Properties of dynamic earthquake ruptures with heterogeneous stress drop, in *Radiated Energy and the Physics of Earthquakes,* Geophysical Monograph Series 170, pp. 255–261, eds McGarr, A., Abercrombie, R., Kanamori, H. & di Toro, G., AGU.

Andrews, D.J., 1973. A numerical study of tectonic stress release by underground explosions, *Bull. seism. Soc. Am.,* **63,** 1375–1391.

Andrews, D.J., 1976a. Rupture propagation with finite stress in antiplane strain, *J. geophys. Res.,* **81,** 3575–3582.

Andrews, D.J., 1976b. Rupture velocity of plane strain shear cracks, *J. geophys. Res.,* **81,** 5679–5687.

Andrews, D.J., 1999. Test of two methods for faulting in finite-difference calculations, *Bull. seism. Soc. Am.,* **89,** 931–937.

Balažovjech, M. & Halada, L., 2006. Effective computation of restoring force vector in FEM, *Kybernetika,* **43,** 767–776.

Barbot, S., Lapusta, N. & Avouac, J.-P., 2012. Under the hood of the earthquake machine: toward predictive modeling of the seismic cycle, *Science,* **336,** 707, doi:10.1126/science.1218796.

Bizzarri, A., 2010. How to Promote earthquake ruptures: different nucleation strategies in a dynamic model with slip-weakening friction, *Bull. seism. Soc. Am.,* **100,** 923–940.

Brietzke, G.B., Cochard, A. & Igel, H., 2009. Importance of bimaterial interfaces for earthquake dynamics and strong ground motion, *Geophys. J. Int.,* **178,** 921–938.

Campillo, M. & Ionescu, I.R., 1997. Initiation of antiplane shear instability under slip dependent friction, *J. geophys. Res.,* **102,** 20 363–20 371.

Dalguer, L.A. & Day, S.M., 2009. Asymmetric rupture of large aspect-ratio faults at bimaterial interface in 3D, *Geophys. Res. Lett.,* **36,** L23307, doi:10.1029/2009GL040303.

Das, S. & Aki, K., 1977. A numerical study of two-dimensional spontaneous rupture propagation, *Geophys. J. R. astr. Soc.,* **50,** 643–668.

Day, S.M., 1977. Finite element analysis of seismic scattering problems, *PhD dissertation,* University of California, San Diego.

Day, S.M., 1982. Three-dimensional simulation of spontaneous rupture: the effect of nonuniform prestress, *Bull. seism. Soc. Am.,* **72**(6), 1881–1902.

Day, S.M., Dalguer, L.A., Lapusta, N. & Liu, Y., 2005. Comparison of finite difference and boundary integral solutions to three-dimensional spontaneous rupture, *J. geophys. Res.,* **110,** B12307, doi:10.1029/2005JB003813.

de la Puente, J., Ampuero, J.-P. & Käser, M., 2009. Dynamic rupture modeling on unstructured meshes using a discontinuous Galerkin method, *J. geophys. Res.,* **114,** B10302, doi:10.1029/2008JB006271.

Duan, B. & Oglesby, D.D., 2006. Heterogeneous fault stresses from previous earthquakes and the effect on dynamics of parallel strike-slip faults, *J. geophys. Res.,* **111,** B05309, doi:10.1029/2005JB004138.

Dumbser, M & Käser, M., 2006. An arbitrary high order discontinuous Galerkin method for elastic waves on unstructured meshes, II: the three-dimensional case, *Geophys. J. Int.,* **167,** 319–336.

Dunham, E.M., 2007. Conditions governing the occurrence of supershear ruptures under slip weakening friction, *J. geophys. Res.,* **112,** B07302, doi:10.1029/2006JB004717.

Favreau, P., Campillo, M. & Ionescu, I.R., 1999. Initiation of in-plane shear instability under slip-dependent friction, *Bull. seism. Soc. Am.,* **89**(5), 1280–1295.

Favreau, P., Campillo, M. & Ionescu, I.R., 2002. Initiation of shear instability in three-dimensional elastodynamics, *J. geophys. Res.,* **107,** doi:10.1029/2001JB000448.

Galis, M. & Moczo P. & Kristek, J., 2008. A 3-D hybrid finite-differenceï finite-element viscoelastic modeling of seismic wave motion, *Geophys. J. Int.,* **175,** 153–184.

Galis, M., Moczo, P., Kristek, J. & Kristeková, M., 2010. An adaptive smoothing algorithm in the TSN modelling of rupture propagation with the linear slip-weakening friction law, *Geophys. J. Int.,* **180,** 418–432.

Garagash, D.I. & Germanovich, L.N., 2012. Nucleation and arrest of dynamic slip on a pressurized fault, *J. geophys. Res. Solid Earth,* **117,** B10310, doi:10.1029/2012JB009209.

Harris, R.A. *et al.,* 2009. The SCEC/USGS dynamic earthquake rupture code verification exercise, *Seismol. Res. Lett.,* **80,** 119–126.

Ida, Y., 1972. Cohesive force across the tip of a longitudinal-shear crack and Griffith's specific surface energy, *J. geophys. Res.,* **77,** 3796–3805.

Kammer, D.S., Radiguet, M., Ampuero, J.-P. & Molinari, J.-F., 2014. Linear elastic fracture mechanics predicts the propagation distance of frictional slip, *Tribol. Lett.,* in press.

Kanwal, R.P., 1983. Generalized functions: theory and technique, in *Mathematics in Science and Engineering,* Vol. 171, ed. Bellman, R., Academic Press.

Liu, Y. & Lapusta, N., 2008. Transition of mode II cracks from sub-Rayleigh to intersonic speeds in the presence of favorable heterogeneities, *J. Mech. Phys. Solid.,* **56,** 25–50.

Moczo, P., Kristek, J., Galis, M., Pažák, P. & Balažovjech, M., 2007. The finite-difference and finite-element modeling of seismic wave propagation and earthquake motion, *Acta Physica Slovaca,* **57,** 177–406.

Moczo, P., Kristek, J. & Galis, M., 2014. *The Finite-difference Modelling of Earthquake Motions: Waves and Ruptures,* Cambridge Univ. Press.

Palmer, A.C. & Rice, J.R., 1973. The growth of slip surfaces in the progressive failure of overconsolidated clay slopes, *Proc. R. Soc. Lond.,* A, **332,** 527–548.

Pelties, C., de la Puente, J., Ampuero, J.-P., Brietzke, G.B. & Käser, M., 2012. Three-dimensional dynamic rupture simulation with a high-order discontinuous Galerkin method on unstructured tetrahedral meshes, *J. geophys. Res.,* **117,** B02309, doi:10.1029/2011JB008857.

Pelties, C., Gabriel, A.-A. & Ampuero, J.-P., 2013. Verification of an ADER-DG method for complex dynamic rupture problems, *Geosci. Model Dev. Discuss.,* **6,** 5981–6034.

Rice, J.R. & Uenishi, K., 2010. Rupture nucleation on an interface with a power-law relation between stress and displacement discontinuity, *Int. J. Fract.,* **163**(1–2), 1–13.

Ripperger, J., Ampuero, J.-P., Mai, P.M. & Giardini, D., 2007. Earthquake source characteristics from dynamic rupture with constrained stochastic fault stress, *J. geophys. Res.,* **112,** B04311, doi:10.1029/2006JB004515.

Ripperger, J., Mai, P.M. & Ampuero, J.-P., 2008. Variability of near-field ground motion from dynamic earthquake rupture simulations, *Bull. seism. Soc. Am.,* **98**(3), 1207–1228.

Rubin, A.M. & Ampuero, J.-P., 2005. Earthquake nucleation on (aging) rate-and-state faults, *J. geophys. Res.,* **110,** B11312, doi:10.1029/2005JB003686

Rubinstein, S.M., Cohen, G. & Fineberg, J., 2007. Dynamics of precursors to frictional sliding, *Phys. Rev. Lett.,* **98**(22), 226103, doi:10.1103/PhysRevLett.98.226103.

Uenishi, K., 2009. On the mechanical destabilization of a three-dimensional displacement-softening plane of weakness, in *Proceedings of the 38th Symposium on Rock Mechanics,* Tokyo, Japan, 8–9 January 2009, pp. 332–337, Committee on Rock Mechanics, The Japan Society of Civil Engineers, Tokyo, Japan.

Uenishi, K. & Rice, J.R., 2003. Universal nucleation length for slipweakening rupture instability under nonuniform fault loading, *J. geophys. Res.,* **108**(B1), 2042, doi:10.1029/2001JB001681.

Uenishi, K. & Rice, J.R., 2004. Three-dimensional rupture instability of a slip-weakening fault under heterogeneous loading, *EOS, Trans. Am. geophys. Un.,* **85**(47), Fall Meet. Suppl., Abstract S13E-04.

Viesca, R.C. & Rice, J.R., 2012. Nucleation of slip-weakening rupture instability in landslides by localized increase of pore pressure, *J. geophys. Res.,* **117,** B03104, doi:10.1029/2011JB008866.

APPENDIX A: CRITICAL SIZE FOR RUNAWAY RUPTURE UNDER LOW BACKGROUND STRESS

Here we derive estimates of the critical initiation area in a fault with low initial stress (high *S* value) based on the Griffith crack equilibrium criterion and small-scale-yielding fracture mechanics. Following the approach of Ripperger *et al.* (2007, Appendix B), we adopt the following simplifying assumptions and approximations.

(i) The rupture is approximately circular, with radius R.

(ii) The initial stress distribution is axisymmetric, $\tau_0(r)$, where r is the distance to the crack centre.

(iii) Stress overshoot is ignored, hence the stress drop is $\Delta\tau(r) = \tau_0(r) - \tau_d$.

(iv) The static stress intensity factor averaged along the crack rim is approximated by the expression for tensile (mode I) cracks,

$$K_0(R) = \frac{2}{\sqrt{\pi R}} \int_0^R \frac{\Delta\tau(r)}{\sqrt{R^2 - r^2}} \, r \, dr. \tag{A1}$$

(v) The details of weakening inside the process zone are ignored and the rupture criterion is based on the fracture toughness K_c, related to the slip-weakening fracture energy by

$$G_c = \frac{1}{2}(\tau_s - \tau_d)D_c = \frac{1}{2\mu}K_c^2. \tag{A2}$$

(vi) The crack is at rest if $\eta \cdot K_0 = K_c$, where the adjustable factor η is a proxy to account for the differences between modes I, II and III, the departures from circularity, the effect of dynamic overshoot, etc.

Next, we determine the conditions for static equilibrium of a circular crack under non-uniform loading, consisting of a concentrated stress over a uniform background stress. We consider a circular overstressed asperity of radius a and stress τ_0^i.

If $a \ll R$, we can approximate the stress in excess of the background stress as a point load, that is, $\Delta\tau(r) = \Delta\tau_0 + F\delta(r)/(2\pi r)$ where $\Delta\tau_0 = \tau_0 - \tau_d$ is the background stress drop and the amplitude of the point load is

$$F = \pi a^2 \left(\tau_0^i - \tau_0\right). \tag{A3}$$

Note that the definition of the delta function in polar coordinates in the form $\delta(r)/(2\pi r)$ is consistent with the assumption that $\int_0^R \delta(r)dr = 1$ (e.g. Kanwal 1983). Based on eq. (A1), the average stress intensity factor is

$$K_0(R) = \frac{F}{(\pi R)^{3/2}} + 2\Delta\tau_0\sqrt{\frac{R}{\pi}}. \tag{A4}$$

This function of R tends to ∞ at $R = 0$ and ∞ and has one minimum given by

$$K_{\min} = 8 \left[\frac{F \Delta\tau_0^3}{2\,(3\,\pi)^3} \right]^{1/4}. \tag{A5}$$

A stable equilibrium crack (a solution to $\eta \cdot K_0(R) = K_c$) exists only if $\eta \cdot K_{\min} \leq K_c$. Combined with eq. (A3), this yields the following condition:

$$\pi a^2 \leq A_1 = \frac{(3\pi)^3}{2^{11}} \left(\frac{\mu D_c}{\eta} \right)^2 \frac{(\tau_s - \tau_d)^2}{(\tau_0^i - \tau_0)\Delta\tau_0^3}. \tag{A6}$$

For an arbitrary value of $a < R$, eq. (A1) yields

$$K_0(R) = \frac{2}{\sqrt{\pi}}(\tau_0 - \tau_d)\sqrt{a}\; f(R/a, \gamma), \tag{A7}$$

where

$$\gamma = (\tau_0^i - \tau_0)/(\tau_0 - \tau_d) \tag{A8}$$

and

$$f(x, \gamma) = \sqrt{x}\left[1 + \gamma(1 - \sqrt{1 - 1/x^2}) \right]. \tag{A9}$$

The minimum of $K_0(R)$ has the following form:

$$K_{\min} = 2\sqrt{\frac{a}{\pi}}(\tau_0 - \tau_d)f_{\min}(\gamma), \tag{A10}$$

where $f_{\min}(\gamma) = \min_x f(x, \gamma)$. Deriving $f_{\min}$ as a function of γ involves some algebra and does not seem to yield a compact expression, so we compute it by numerical minimization. The condition $\eta \cdot K_{\min} \leq K_c$ yields:

$$\pi a^2 \leq A_2 = \frac{\pi^3}{2^4} \left(\frac{\mu D_c}{\eta} \right)^2 \frac{(\tau_s - \tau_d)^2}{(\tau_0 - \tau_d)^4 f_{\min}^4}. \tag{A11}$$

We find that with the adjustable factor $\eta = 1$ both estimates, A_1 and A_2, fit our numerical results very well. For this choice of the adjustable factor, eq. (A2) corresponds to the energy flux in mode III, $G_{III} = K^2/(2\mu)$. In 2-D, the critical half-lengths for mode III are smaller than those for mode II. The energy flux for mode II is $G_{II} = (1 - \nu)K^2/(2\mu)$, which corresponds to $\eta = \sqrt{1 - \nu}$. However, with this choice of η, both estimates predict larger critical area than observed in our numerical results.

Our numerical results suggest $\eta = 1$, indicating that mode III is more important for the nucleation of rupture in 3-D than mode II. However, to verify this conjecture mode II and III expressions for the the stress intensity factor K along the crack rim need to be derived (currently we are using mode I expression averaged along the crack rim), which is beyond the scope of this study.

APPENDIX B: EFFECTS OF INCREASING OVERSTRESS FROM $0.005 \cdot \Delta\tau_E$ TO $0.05 \cdot \Delta\tau_E$

As noted in Section 5 we perform a detailed analysis of the effects caused by increasing the overstress from $0.005 \cdot \Delta\tau_E$ to $0.05 \cdot \Delta\tau_E$ (i.e. corresponding to fixed increments of the overstress used in Section 5.2). We consider only two limiting configurations, with $S = 0.1$ and 2.0, with square initiation zone and with element size $h = 100$ m. We analyse rupture time, rupture speed, traction and slip rate.

Comparison of rupture time can reveal changes in the shape of the rupture. However, rupture time is a cumulative quantity, and
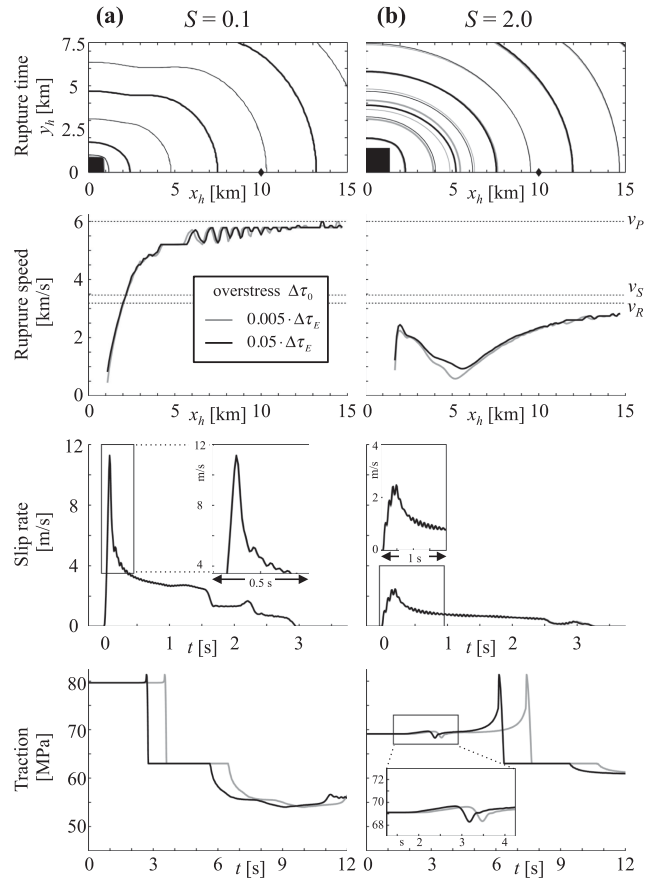

Figure B1. Illustration of effects of increasing overstress from 0.005 to $0.05 \cdot \Delta\tau_E$. For the low-strength case (a) the interval between thick contours in rupture time plots is 1 s and consequently the interval between thick and thin contours is 0.5 s. For the high-strength case (b) the intervals are 2 and 1 s, respectively. x_h and y_h denote distance from hypocentre. The diamond depicts the receiver position on the fault plane.

therefore any differences near the initiation zone remain visible over the entire fault plane, complicating the comparison of rupture shapes. To reduce this effect the rupture time is modified such that the solution with higher overstress matches the rupture time of the solution with lower overstress at the selected receiver position (diamond in Fig. B1).

We include rupture speed in the in-plane direction in the analysis to help us understand the differences in observed rupture time. Rupture speed, v_r, is computed as the inverse of spatial gradient of rupture time T_r:

$$v_r = \frac{1}{|\nabla T_r|}. \tag{B1}$$

To reduce artefacts caused by the finite time-step we applied moving window average to rupture time. Consequently, the rupture speed also acquires values from range $[v_R, v_S]$. Note that this does not affect our analysis as we are only investigating differences in solutions.

Comparison of tractions provides the possibility to compare the stress variation due to propagating hypocentral S wave for high-strength configuration. In addition, it provides visual reference of differences in rupture time.

Slip rate histories reflect details of the break-down process, and hence a detailed comparison of shape and peak amplitudes is important. Therefore, we plot slip rates using relative time, starting at the rupture time.

Results for $S = 0.1$ (Fig. B1a) show very good agreement except for the traction for which we observe significant difference in rupture time; the solution with higher overstress arrives 0.9 s earlier.

Results for $S = 2.0$ (Fig. B1b) are more complicated but overall show good agreement. We can see differences in rupture time as well as in rupture speed. However, these differences vanish at distance $\approx 7 - 8$ km $\approx 10 - 11.5 \cdot L_{\text{fric}}$ from the hypocentre. Comparison of tractions shows again differences in rupture time; the peak stress arrives 1.3 s earlier with higher overstress. In the zoomed-in image we observe also difference in (apparent) rupture time of the stress variation related to propagating S wave along the fault. The rupture time of the stress variation is the same in both solutions, only the shape is less steep in the solution with lower overstress leading to apparent difference in rupture time. Nevertheless, the slip rates show very good agreement.

Overall, this analysis indicates that variations of overstress smaller than $0.05 \cdot \Delta \tau_E$ do not affect significantly the resulting self-sustained rupture propagation.

APPENDIX C: EFFECTS OF USING HIGHER OVERSTRESS SCALED ACCORDING TO CHOSEN INITIATION AREA

We investigate in detail the effects caused by initiation of rupture using higher overstress in two sets of simulations: (1) 'slightly overcritical' set with initiation area barely larger than the critical area for each overstress value (according to results in Fig. 12) and (2) 'supercritical' set with fixed initiation area A_{init}^0 corresponding to the lowest considered overstress $\Delta \tau_0 = 0.005 \cdot \Delta \tau_E$. As noted in Section 5, we perform simulations for square initiation zone and element size $h = 100$ m. We analyse the same quantities as in Appendix B for two limit configurations, $S = 0.1$ and 2.0. We expect that the smallest overstress leads to reduced artefacts, consequently, the reference solutions, for this analysis, are those for initiation area A_{init}^0 with overstress $\Delta \tau_0 = 0.005 \cdot \Delta \tau_E$. All numerical results are summarized in Fig. C2 (similar to Fig. C1).

Fig. C1(a) compares four supercritical solutions for $S = 0.1$ and Fig. C1(b) compares four slightly overcritical solutions. Rupture time and rupture speed plots in Figs C1(a) and (b) show very good agreement, with only small differences near initiation zone. The differences, better visible in Fig. C1(a), occur only for points less
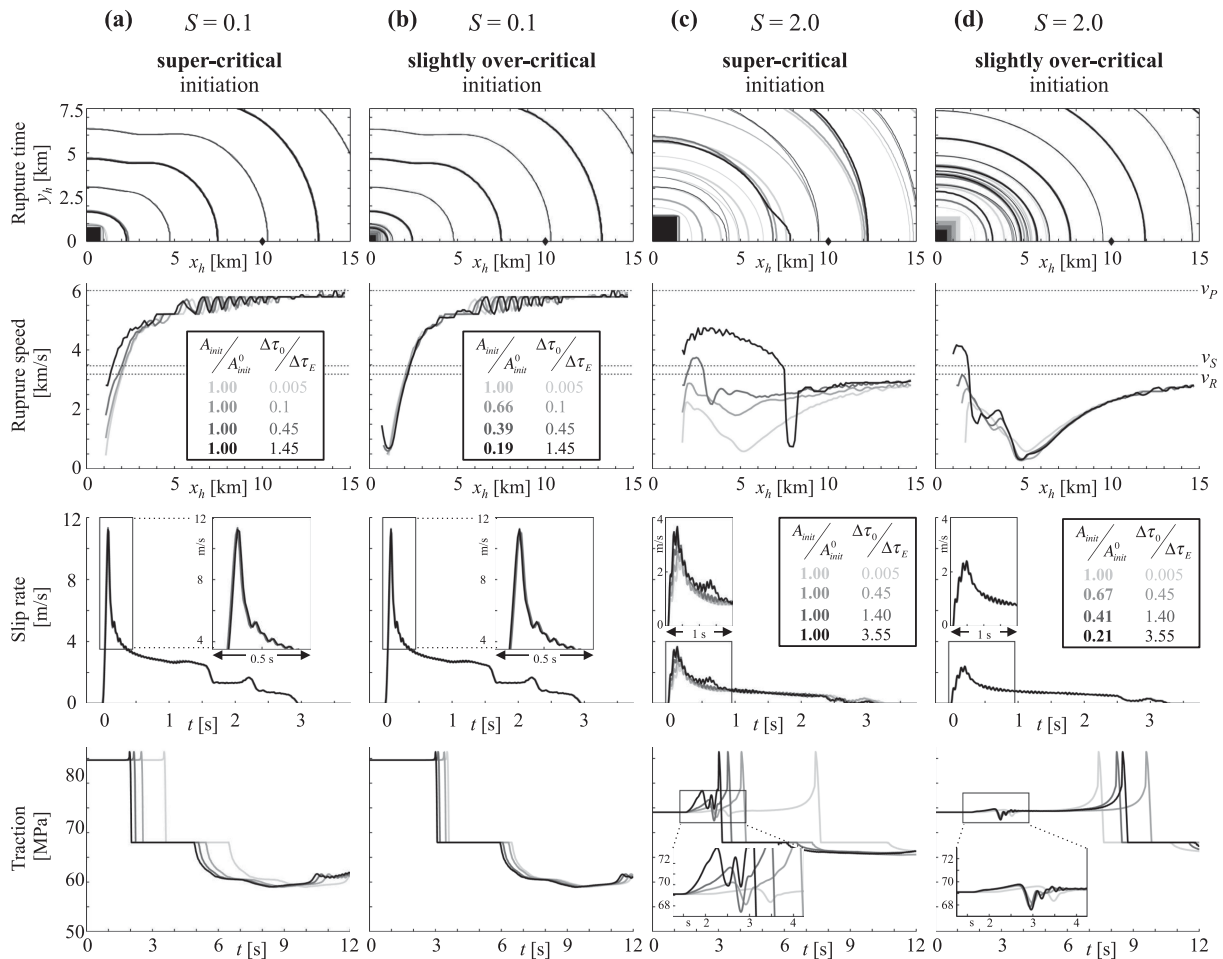
Figure C1. Illustration of the effects of overstress on (i) rupture time, (ii) rupture speed (in the in-plane direction), (iii) x-component of the slip rate and (iv) x-component of the traction. Results with supercritical and slightly overcritical initiation for low-strength configuration are compared in (a) and (b), respectively. Similarly, results for high-strength configuration are summarized in (c) and (d). The effective size of the (square) initiation zone is indicated in the rupture time plots. A_{init}^0 denotes the area of the initiation zone with overstress $\Delta \tau_0 = 0.005 \cdot \Delta \tau_E$.

than $A_{init}^0/2$ from hypocentre. On the other hand, comparison of slip rates show very good agreement in both cases, with negligible differences between solutions.

Comparing Figs C1(c) and (d) we observe that in case of the high-strength configuration, $S = 2.0$, the effects are much stronger than in the low-strength configuration and, moreover, they significantly vary between the figures. Therefore we address the two cases separately.

The supercritical solutions for $S = 2.0$ are compared in Fig. C1(c). Rupture time plots show large differences and, in contrast to the low-strength case, the differences are not localized at shorter distances from the hypocentre. While at shorter distances from the hypocentre, bumps in contours of the solutions with $3.55 \cdot \Delta\tau_E$ (i.e. largest considered overstress) indicate a transition to supershear rupture speed, at larger distances the rupture tends to be more circular when higher overstress is applied. The more circular shape indicates variation of rupture speed in the antiplane direction. In addition, rupture speed shows significant differences. Even after propagating to the boundary of considered fault plane (i.e. 15 km) the rupture initiated with higher overstress propagates with higher speed than ruptures initiated with lower overstress. Moreover, the overstresses $3.55 \cdot \Delta\tau_E$ and $1.40 \cdot \Delta\tau_E$ lead to supershear rupture over a portion of the fault plane, although in both cases the rupture speed eventually drops down to sub-Rayleigh speed. This time we see significant differences also in the slip rate histories— higher overstress leads to larger amplitudes and to changes in shape of the slip rate peak. We also observe significant changes of the traction peaks corresponding to the *S*-wave propagating along the fault (peaks occurring before the static strength is reached). Particularly, the large amplitude of this peak may eventually lead to the supershear transition for a configuration when the transition is not expected.

As shown in Fig. C1(d), in the slightly overcritical case the effects on rupture propagation are small (compared with Fig. C1c). The rupture time plots show significant variations only at shorter distances from the hypocentre, and, in contrast with the previous case, the agreement is very good at larger distances and also the rupture speed agrees well. Significant differences can be spotted only in close vicinity of the hypocentre, but soon after initiation the rupture speed varies consistently in all cases, though small differences between solutions are visible. At larger distances from the hypocentre we observe very good agreement between all solutions. Slip rate plot shows excellent agreement and even detail image shows no significant differences. However, the zoomed-in image showing the stress variation due to propagating *S* wave reveals that the reference solution is separated from the other three cases. Despite the amplitudes of these solutions for higher overstress are larger than in the reference case, they are much lower than in case of fixed initiation area (Fig. C1c).

As discussed in Appendix D, the differences in rupture times for both configurations, $S = 0.1$ as well as $S = 2.0$, indicate that higher overstress leads to shorter duration, assuming fixed initiation area. This is also seen in traction plots in Figs C1(a) and (c) for fixed initiation area. However, this does not apply to the remaining two cases (Figs C1b and d) because we varied not only overstress but also initiation area. As discussed in Section 5, to find the critical overstress we consider fixed variations of the overstress, $0.05 \cdot \Delta\tau_E$. Consequently, the critical overstress is obtained with uncertainty— in the worst case the observed critical overstress may be almost $0.05 \cdot \Delta\tau_E$ larger then the minimum required overstress. As shown in Appendix D, even such small variation of overstress may lead to significant difference in duration of initiation in low- and high-strength configurations. The differences in rupture times for low-strength

configuration ($S = 0.1$) are within limits observed in Fig. B1, therefore we attribute them to uncertainty in estimating the critical overstress. However, rupture times for high-strength configuration are not consistent with this hypothesis, because the difference between first and last rupture is larger than in Fig. B1 for overstresses $0.05 \cdot \Delta\tau_E$ and $0.005 \cdot \Delta\tau_E$. Moreover, we observe that the solution with smallest overstress arrives first. This would indicate that the difference between critical overstress and the minimum required overstress is in all cases less than $0.005 \cdot \Delta\tau_E$, which is very unlikely. Therefore, we conjecture that this behaviour is a consequence of two opposing effects: (i) smaller initiation area leads to longer duration of the initiation, (ii) higher overstress leads to shorter duration of the initiation.

In summary, our results reveal that slightly overcritical initiation, that is, when the initiation area is set barely larger then critical area for considered overstress, does not produce strong artefacts even if the absolute value of the overstress is rather large.

APPENDIX D: EFFECTS OF USING LARGER INITIATION AREA OR HIGHER OVERSTRESS TO SHORTEN THE DURATION OF THE INITIATION

In Section 6, we analysed the relative difference in rupture time, ΔT_r, and the relative difference of peak slip rate amplitude, $\Delta\dot{u}_{max}$, and showed that using either larger area or higher overstress than their corresponding critical values leads to shorter duration of the initiation. Here we support the conclusion by the analysis of rupture shape, rupture speed, traction and slip rate time histories.

As mentioned in Section 6, we perform simulations for square initiation zone and element size $h = 100$ m. All results are summarized in Fig. D1 (note similar layout as Fig. C1). We consider solutions obtained with smallest considered overstress, $\Delta\tau_0/\Delta\tau_E = 0.005$, and the smallest initiation area, A_i^0, as reference solutions.

Numerical results for the low-strength case (Figs D1a and b) show generally good agreement of all analysed quantities, except rupture time, which shows that the application of initiation area $A_{init} \geq 2.2 \cdot A_{init}^0$ leads to significant changes in rupture shape. Moreover, previous analysis of ΔT_r (Section 6) showed that higher overstress provides more pronounced shortening of the duration. Therefore, our analysis suggests that for low-strength configurations application of higher overstress is preferable as the shortening of duration is more pronounced and it introduces less artefacts than using larger initiation zone.

Numerical results for the high-strength configuration (Figs D1c and d) show much larger variability than for low-strength configuration. First, we examine the effects of larger initiation zone, that is, Fig. 13(c). Initiation areas $A_{init} \geq 1.2 \cdot A_{init}^0$ lead to significant variations of rupture shape as indicated by the rupture time comparisons. Also rupture speed shows significant differences. In contrast with the low-strength case, we observe these differences also at large distances from hypocentre. Moreover, we can identify two branches in rupture speed. Even though the branches eventually converge, using $A_{init} \geq 1.2 \cdot A_{init}^0$ may be associated with an increase of numerical artefacts. The slip-rate comparison shows not only differences in shape and peak amplitude but also larger amplitudes of spurious high-frequency oscillations. Significant differences towards the end of the slip-rate function are associated with changes of the shape of the rupture (as indicated by rupture time plots). We recall that the first healing occurs due to a healing pulse propagating from longer edge of the fault while a second
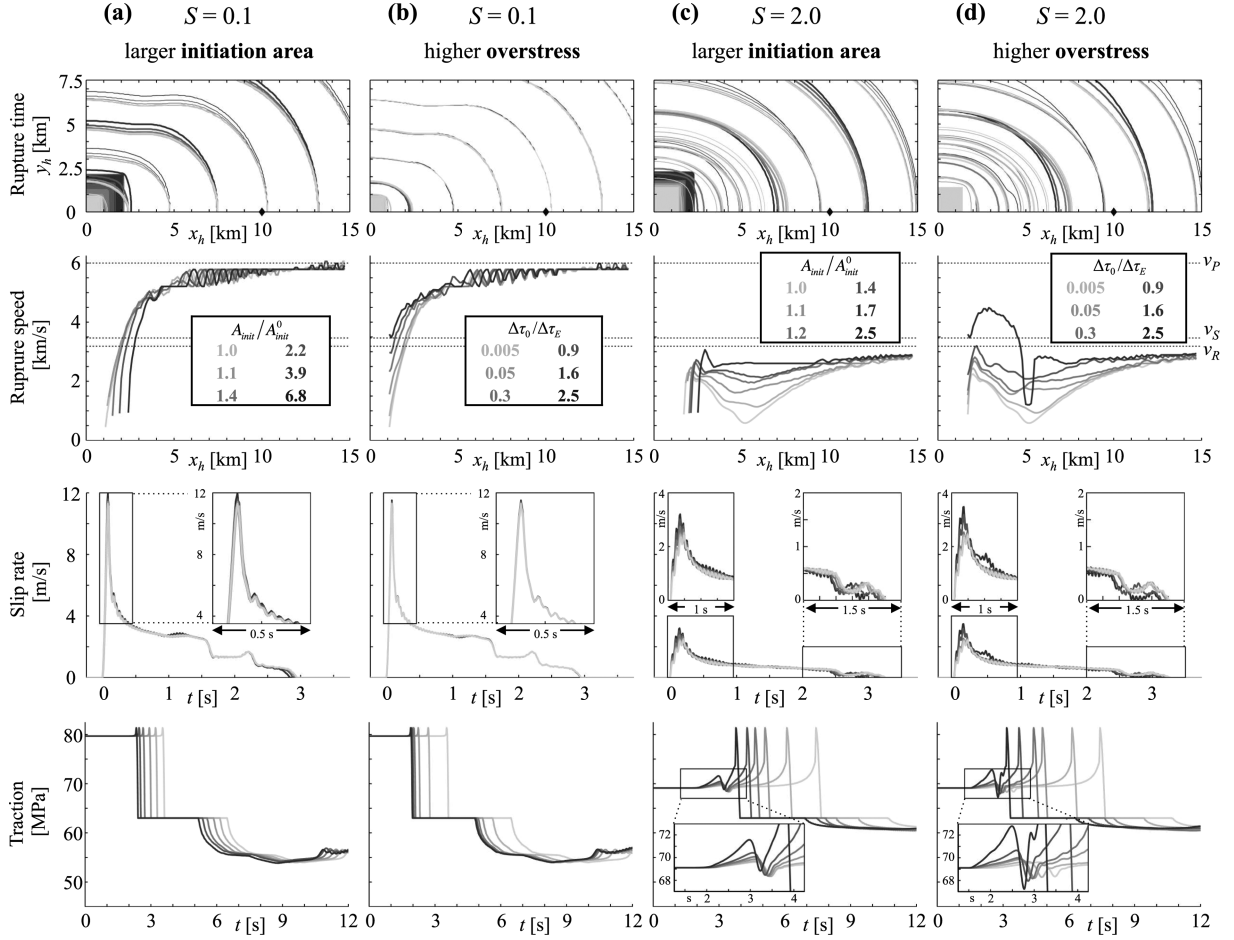
Figure D1. Illustration of the effects associated with application of larger initiation area or higher overstress to shorten the duration of the initiation on (i) rupture time, (ii) rupture speed (in the in-plane direction), (iii) *x*-component of the slip rate and (iv) *x*-component of the traction. Results for low-strength configuration with increasing initiation area are shown in (a) and with increasing overstress in (b). Analogously, results for for high-strength configuration are summarized in (c) and (d). Note similar layout as in Fig. C1.

healing episode is caused by healing pulse from shorter edge. Comparison of stress variation due to propagating *S* wave shows only negligible differences for $A_{\text{init}} \leq 1.4 \cdot A_{\text{init}}^0$. We conclude that using initiation area smaller than $A_{\text{init}} \lesssim 1.2 \cdot A_{\text{init}}^0$ leads to a significant decrease of initiation duration without introducing strong numerical artefacts.

Comparison of rupture time plots for the case of higher overstress (Fig. D1d) reveals changes in rupture shape caused by overstress $\Delta\tau_0 \geq 1.6 \cdot \Delta\tau_E$. For overstress $\Delta\tau_0 = 2.5 \cdot \Delta\tau_E$ we observe undulations on the contour indicating supershear rupture speed. In addition, the comparison of rupture speed reveals two branches suggesting to use overstress $\Delta\tau_0 \leq 0.9 \cdot \Delta\tau_E$. Slip rate histories show larger differences as in the case of larger initiation area. As indicated by analysis of $\Delta\dot{u}_{\text{max}}$ in Section 6, overstress $\Delta\tau_0 \leq 0.3 \cdot \Delta\tau_E$ leads to small errors in peak amplitude ($\Delta\dot{u}_{\text{max}} < 5$ per cent). However, further increase of the overstress is associated with a steep gradient

of $\Delta\dot{u}_{\text{max}}$ (the secondary peak in the case of $\Delta\tau_0 = 2.5 \cdot \Delta\tau_E$ is likely a consequence of supershear rupture that occurred near the IZ). Comparison of tractions also shows generally stronger effects than observed in the case of larger initiation zone. However, detailed comparison of the stress variations associated with propagating *S* wave reveals only slight changes of the apparent rupture time as well as of the time when maximum is reached if $\Delta\tau_0 \leq 0.3 \cdot \Delta\tau_E$. At the same time, the amplitude of the peak exhibits only negligible variations for $\Delta\tau_0 \leq 0.3 \cdot \Delta\tau_E$.

In summary, our results and analysis suggest that for lower-strength configurations, it is more efficient to apply higher overstress, $\Delta\tau_0 \leq \Delta\tau_E$ to shorten the duration of initiation without introducing strong artefacts. On the other hand, application of larger initiation area, $A_{\text{init}} \lesssim 1.2 \cdot A_{\text{init}}^0$ seems to be more suitable for higher-strength configurations than application of higher overstress.